A fundamental work on THz measurement techniques

for application to steel manufacturing processes.

Dissertation
zur Erlangung des Doktorgrades
der Naturwissenschaften

Vorgelegt beim Fachbereich Physik
der Johann Wolfgang Goethe-Universität
in Frankfurt am Main

von: Noboru Hasegawa
aus: Kobe (Japan)

Frankfurt am Main 2004
(DF1)

vom Fachbereich ……………………………………………………………………………… der
Johann Wolfgang Goethe – Universität als Dissertation angenommen.

Dekan : ....

Gutachter : ....

Datum der Disputation : ....

A table of contents

1. Introduction

The terahertz (THz) waves had not been obtained except by a huge system, such as a free electron laser, until an invention of a photo-mixing technique at Bell laboratory in 1984 [1]. The first method using the Auston switch could generate up to 1 THz [2]. After then, as a result of some efforts for extending the frequency limit, a combination of antennas for the generation and the detection reached several THz [3, 4]. This technique has developed, so far, with taking a form of filling up the so-called 'THz gap'. At the same time, a lot of researches have been trying to increase the output power as well [5-7]. In the 1990s, a big advantage in the frequency band was brought by non-linear optical methods [8-11]. The technique led to drastically expand the frequency region and recently to realize a measurement up to 41 THz [12]. On the other hand, some efforts have yielded new generation and detection methods from other approaches, a CW-THz as well as the pulse generation [13-19].

Especially, a THz luminescence and a laser, originated in a research on the Bloch oscillator, are recently generated from a quantum cascade structure, even at an only low temperature of 60 K [20-22]. This research attracts a lot of attention, because it would be a breakthrough for the THz technique to become widespread into industrial area as well as research, in a point of low costs and easier operations.

It is naturally thought that a technology of short pulse lasers has helped the THz field to be developed. As a background of an appearance of a stable Ti:sapphire laser and a high power chirped pulse amplification (CPA) laser, instead of a dye laser, a lot of concentration on the techniques of a pulse compression and amplification have been done. [23]

Viewed from an application side, the THz technique has come into the limelight as a promising measurement method. A discovery of absorption peaks of a protein and a DNA in the THz region is promoting to put the technique into practice in the field of medicine and pharmaceutical science from several years ago [24-27]. It is also known that some absorption of light polar-molecules exist in the region, therefore, some ideas of gas and water content monitoring in the chemical and the food industries are proposed [28-32]. Furthermore, a lot of reports, such as measurements of carrier distribution in semiconductors, refractive index of a thin film and an object shape as radar, indicate that this technique would have a wide range of application [33-37].

I believe that it is worth challenging to apply it into the steel-making industry, due to its unique advantages. The THz wavelength of 30-300 μ m can cope with both independence of a surface roughness of steel products and a detection with a sub-millimeter precision, for a remote surface inspection. There is also a possibility that

it can measure thickness or dielectric constants of relatively high conductive materials, because of a high permeability against non-polar dielectric materials, short pulse detection and with a high signal-to-noise ratio of 10^{3-5}. Furthermore, there is a possibility that it could be applicable to a measurement at high temperature, for less influence by a thermal radiation, compared with the visible and infrared light. These ideas have motivated me to start this THz work.

2. Foundation

The typical THz technique applicable to a spectroscopic measurement is required the following four elements; (i) a short pulse laser which has less than a sub-picosecond pulse width with high peak power (10 GW), (ii) a conversion mechanism of the visible laser into THz waves, for the THz generation, (iii) a THz detection and (iv) an optical system for its propagation. In this chapter, I mention the construction and the principle of the representative generation and detection methods and a result of simple calculations that the THz waves have strong dependence on their wavelengths in spatially propagating with an usual optical system, compared with the visible or infrared light.

2.1. THz generation
2.1.1. CPA laser system

A typical CPA laser consists of three functions of a pulse expansion, an amplification and a compression, shown in Fig. 2.1. These make it possible to increase the output power by 100 times with the same pulse width as an incident laser.
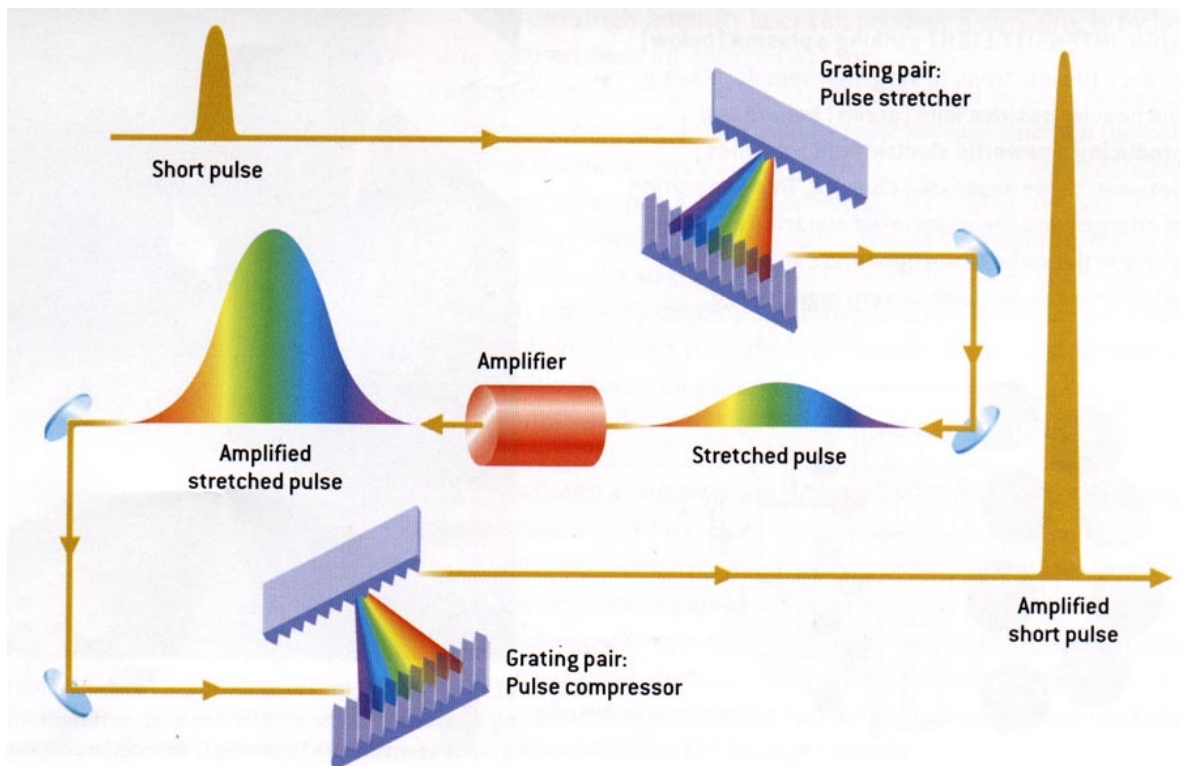

Figure 2.1. Configuration of a pulsed laser compression with a CPA technique [96].

(a) Pulse stretcher: This expands an incident pulse from a Ti:sapphire laser (in time domain) by 10^4 times. Several ways have been proposed as a stretcher, for example, a

1:1 telescope, a grating pair, a pair of prism, and an optical fiber [38-40]. The former three generate the chirped pulse through the spatial expansion, and the last one by non-linear effects, such as a self-phase modulation or group velocity dispersion. However, they have a common feature in that they generate the chirped pulse, thus the lower frequency components of the light travel ahead of the higher ones.

(b) Amplifier: This simply means a laser medium. Without a stretched pulse, a couple of problems might be occurred, in that there are possibilities to destroy the material by an intense focusing, caused from a self-focusing effect, and to decrease the conversion efficiency with a saturation. The stretched pulse makes it possible to amplify the incident beam with a big gain and without a spatial beam expansion.

(c) Compressor: This is the inversed process of (a), and compresses the amplified pulse (in time domain). In ordinary circumstances, the same method is applied as the selected stretcher in (a).

2.1.2. Conversion to THz waves

As mentioned in the chapter 1, there are a lot of the THz generation methods in these days. Among them, I briefly state here the typical configurations and their principles of the photo-mixing and the optical rectification which have become the standards in the THz generation field.

2.1.2.1. Biased antenna

Fig. 2.2 illustrates an example of the most primitive antennas has a pair of electrodes, parallel established on a semiconductor substrate by a lithographic process. A visible laser pulse is illuminated in the gap between the electrodes under a circumstance that an electric bias of 1-10 kV/cm is applied. If the photon energy of the laser is beyond the band gap of the substrate material, conductive carriers (electrons and holes) are excited on its surface by the absorption process, in a quite short time. A bipolar radiation is induced from the accelerated carriers by the bias. The radiation theory of electric-magnetic waves into the air, based on the Maxwell equations, estimates that the output electric field is proportional to the derivative of the surface current in the far-field [41, 42].
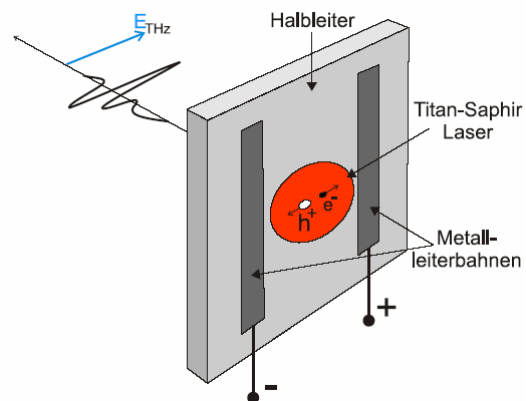

Figure 2.2. THz generation scheme from a dipole antenna [95].

In general, the frequency dependence of the generation is determined by the size, the shape of the electrodes and a carrier mobility of the substrate material and so on. So far, a lot of antennas are proposed, such as a bow-tie, a large-aperture antenna with some variations of the substrates, e.g. a silicon-on-sapphire (SOS) and a GaAs thin film grown at low temperature as well as a GaAs crystal [43-48].

2.1.2.2. Optical rectification

In this method, the THz generation is obtained by an optical non-linear effect. Zinc-blend crystals, such as a GaAs and a ZnTe, cut at a specific orientation have the 2nd order non-linear coefficients and their dielectric polarization is expressed by

$$P_i(\Omega) = \varepsilon_0 \int_{\omega_0 - \Delta\omega/2}^{\omega_0 + \Delta\omega/2} d_{ijk}(-\Omega; \omega + \Omega; -\omega) \cdot E_j(\omega + \Omega) E_k^*(\omega) d\omega \qquad (2\text{-}1)$$

where ω_0 is the central frequency, $\Delta\omega$ is the bandwidth of the incident beam, and d_{ijk} refers to the non-linear optical susceptibility tensor elements of the crystal [9]. The frequency Ω ranges from dc to $\Delta\omega$. $E_j(\Omega + \omega)$ and $E_k^*(\omega)$ are the Fourier transforms of the electric field components of the incident beam. The Zinc-blend crystals have a cubic structure with the point group 43m and have only one independent non-vanishing second-order non-linear optical coefficient, namely $d_{14} = d_{25} = d_{36}$. When a visible laser with a pulse width of 100 fs order passes through the crystal, THz wave is generated by a modulation according to its pulse profile (Fig. 2.3).
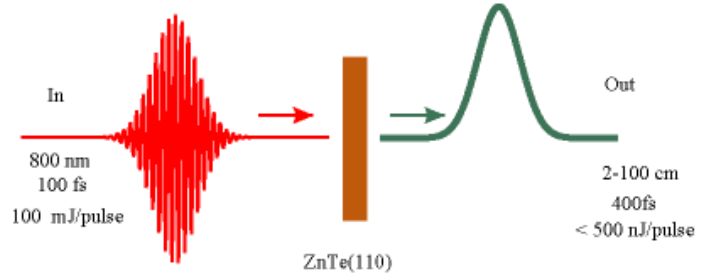
Figure 2.3. Schematic illustration of a photo rectification [97].

In general, there is a trade-off between the THz output gain and the spectral width in the frequency region. When a thicker crystal is applied, the gain is increased in proportion to the thickness, however the frequency range is limited by the phase-mismatch inside the crystal [49]. This is why the frequency components included in the generated THz pulse are lower than the one of the laser pulse itself. For getting higher frequency range, a usage of a surface non-linear effects and a combination of a thinner crystal and a shorter incident pulse are reported [50, 51, 12].

An example of the waveforms generated by each method is shown in Fig. 2.4. The figures (a) and (b) indicate time domain data and their spectrum by a large-aperture antenna, and (c), (d) by an optically non-linear crystal, respectively. The electrodes of the antenna are established on an intrinsic GaAs substrate, and its distance was 30 mm with 3 kV bias. On the other hand, the non-linear crystal is a 1 mm thick ZnTe, cut at (110) orientation. The condition of the input laser is the same for both measurements, the pump and probe pulses of 150 fs duration at a wavelength of 775 nm and a repetition rate of 1 kHz. The detection is also the same, an electro-optic detection. The only difference is what the laser is spatially expanded by a 1:3 telescope, in the latter case. These graphs imply that the optical method has a higher-frequency response.
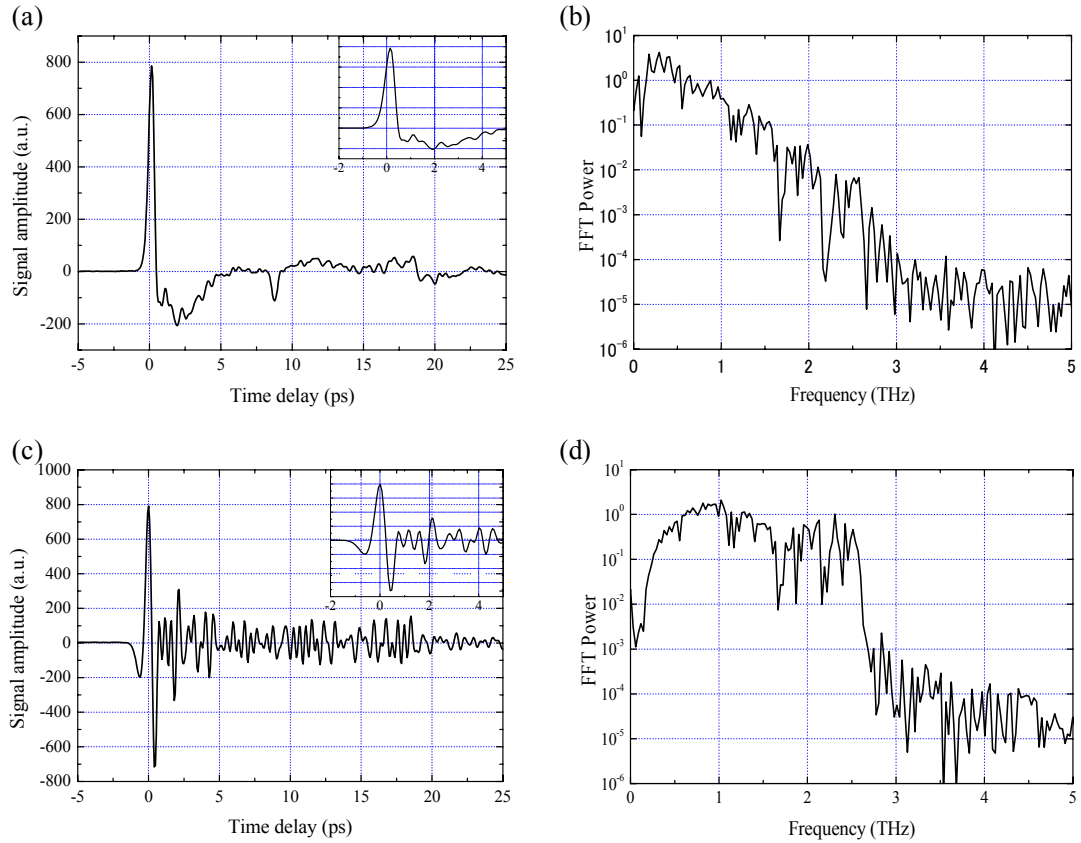

Figure 2.4. (a), (c) THz time domain data, and (b), (d) their Fourier spectra by a large-aperture GaAs emitter, and by an EO emitter, respectively. Zoomed data are shown in the inset of (a) and (c). Both signals are detected by an EO detection.

2.2. THz detection

There exists less method than the THz generation. I mention two typical detections using an antenna and an electro-optic effect.

2.2.1. THz antenna

This detection technique is applied the same shape of the antenna as the THz generation. The different process is to measure the current between the two electrodes instead of applying a high voltage. As shown in Fig. 2.5, visible laser pulses (probe pulses) are focused on the gap of the elect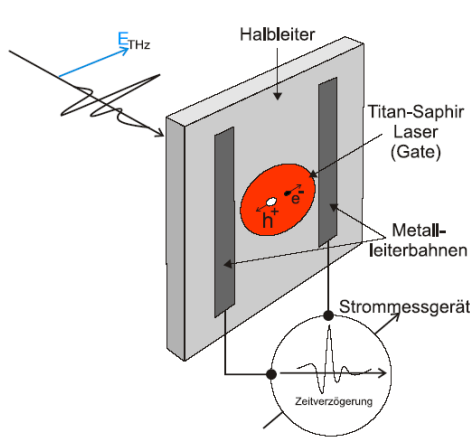rodes, with tuning the delay time between the THz waves and the laser pulses. When the probe pulse overlaps the THz pulse, non-zero current is detected, caused from the movement of the excited carriers by the pump laser. The signal is excited in proportion to the electric field of the THz pulse. On the other hand, the current is not observed without the THz pulse, because of the recombination of the carriers. The THz pulse shape is constructed by a sequential delay of the laser pulse, when the pulse width of the probe beam is sufficiently short, e.g. less than one-tenth of the THz pulse.

Figure 2.5. THz detection scheme by a dipole antenna [95].

2.2.2. Electro-optic detection

A crystal which has an electro-optic (EO) effect, that an external electric field induces a change of its refractive index, depending on the amplitude, is utilized in this method. The refractive index n as a function of the electric field is described as

$$n(E) = n_0 - \frac{1}{2}\mathbf{r}n^3 E - \frac{1}{2}\mathbf{s}n^3 E^2 , \qquad (2\text{-}2)$$

where n_0 is the refractive index without the biased field, $\mathbf{r}$ and $\mathbf{s}$ are the electro-optic coefficients [52]. The changes by the second and third terms are called Pockels- and Kerr-effect, respectively. These values depend on a crystal orientation, as well as a characteristic of the material.

The principle is schematically illustrated in Fig. 2.6. A probe beam is focused onto the EO crystal along the same axis as the THz propagation. The polarization of the THz beam is adjusted parallel to the main axis of the crystal, and the probe beam is rotated by 45 degrees. A quarter wave plate (an analyzer), positioned after the crystal, makes

the probe beam polarization change from linear to circular. Then, the beam is split up into a polarizing beam splitter into the s and p components, which are separately detected by two detectors. In case of no
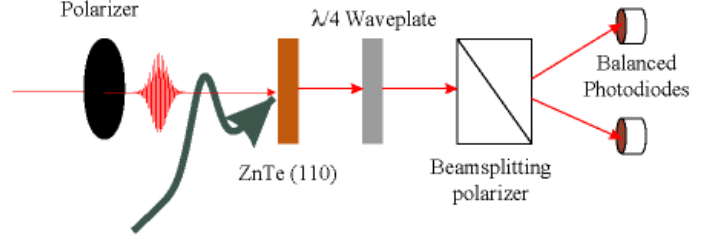

Figure 2.6. Configuration of an EO detection [97].

overlapping with the THz pulse (without the THz-field inside the crystal), signals of 50:50 ratio is received for the perfectly circular polarization. On the other hand, when an overlap of them exists, the prove beam is output with a slightly elliptic polarization. Therefore, this result in an uneven ration of each detected signal intensity. At this time, some time delay $\Delta\phi_{THz}$ yielded between the ordinary and the extraordinary components of the probe pulse in the crystal is proportional to the crystal length and the induced electric field by the THz wave [53]. The electric field and the phase of the THz wave become detectable by adjusting the relative delay time between the probe and the THz pulses.

These two detection methods have also different frequency spectra. It is known that they can detect signals with almost the same signal-to-noise ratio, but the EO detection has wider spectrum, in general [9].

2.3. THz propagation
2.3.1. Theory of Gaussian beam

When the spatial distribution of a beam is described by the Gauss function, in a perpendicular plane to its propagation (z), it is called Gaussian beam, especially basic Gaussian beam in case that its variation is limited to along the radius axis $r = \sqrt{x^2 + y^2}$. The electric field of the basic Gaussian beam is derived from the Maxwell equations to a homogeneous medium without an electric charge;

$$E(x, y, z) = E_0 \frac{\omega_0}{\omega(z)} \exp\left\{-i\left[kz - \tan^{-1}\left(\frac{z}{z_0}\right)\right] - r^2\left(\frac{1}{\omega^2(z)} + \frac{ik}{2R(z)}\right)\right\}, \qquad (2\text{-}3)$$

where $z_0 = \pi\omega_0^2 n / \lambda$ and n is the refractive index of the medium [54]. The $\omega(z)$, what is called a beam spot size, indicates a distance (r) between the center and the position where the amplitude of the electric field is 1/e of the peak. ω_0 is the minimum

spot size at the z=0 (beam waist) position. $R(z)$ represents a curvature of the wave front (a surface with the same phase) at every z position under an assumption that the beam is approximated to a spherical wave. According to Eq. (2-3), the profile of the Gaussian beam is absolutely fixed when ω_0 and its position are specified.

On the other hand, a converting rule at a border between two kinds of media is derived from a propagation rule in a medium with a distribution of square of the refractive index (lens-like);

$$q_2 = \frac{Aq_1 + B}{Cq_1 + D},$$
(2-4)

where the complex beam radius is defined as

$$\frac{1}{q(z)} = \frac{1}{R(z)} + i\frac{\lambda}{\pi n \omega^2(z)}.$$
(2-5)

Especially, when this is applied to a thin lens with a focal length f, a relation between q of medium 1 and 2,

$$\frac{1}{q_2} = \frac{1}{q_1} - \frac{1}{f}$$
(2-6)

($\omega_1 = \omega_2$, $1/R_2 = 1/R_1 - 1/f$), is concluded.

This rule is preserved when the beam passes through more than a couple of lenses. It is worth noting that the complex beam radius is determined only by its wavelength λ, except for $\omega(z)$ and $R(z)$.

2.3.2. Focusing property

Previous to some experiments, I estimated the focusing behavior of the THz wave passing through a 2-f optical configuration, grounded on the propagation theory of the section 2.3.1. Fig. 2.7 (a) shows a schematic illustration of the optical system, simulated the experimental setup in the chapter 3 and 4. The THz beam generated from the emitter E is focused onto the S-plane by the lens L1. After collimated by the lens L2, it is again focused onto the detector position D using the lens L3. Here, all the lenses have the same focal length 120 mm, and the distances among E-L1-S-L2-F-L3-D are all equal to it. The beam radii as a function of position for the 0.39-1.95 THz range and, for your reference, a He-Ne laser wavelength 632.8 nm are shown in Fig. 2.7 (b) and (c). Two cases of the emitted radii 7.5 and 15 mm are included in the calculation. All the cases, they have the same focal position in the calculation, but the size of the beam waist is inclined to be smaller as the wavelength becomes longer. In case of the initial radius 7.5 mm, the focal sizes are millimeter to sub-millimeter order, e.g. 4 mm at 0.39 THz and 0.8 mm at 1.95 THz, and they become almost half when the initial is doubled, indicated

Z

E   L1   S   L2   F   L3   D

E: emitter,   L: lens,
S: sample,   D: detector

(b)

Beam radius (mm)

Distance (mm)

0.39 THz
0.68 THz
0.98 THz
1.37 THz
1.95 THz
Laser

Beam radius (mm)

Distance (mm)

(c)

Beam radius (mm)

Distance (mm)

0.39 THz
0.68 THz
0.98 THz
1.37 THz
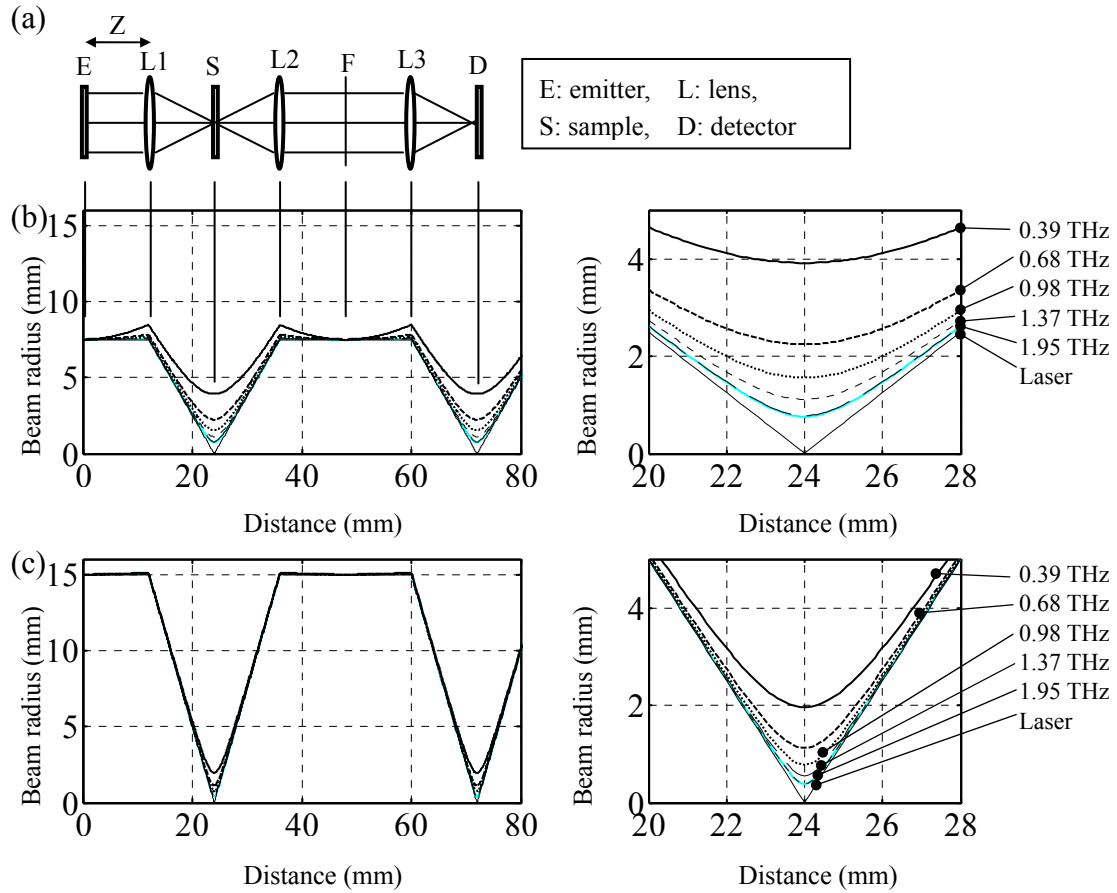1.95 THz
Laser

Beam radius (mm)

Distance (mm)

Figure 2.7. (a) Simplified illustration of a 2-f optical configuration, (b) a calculation results with an initial beam radius of 7.5 mm, in frequencies of 0.39, 0.68, 0.98, 1.37, 1.95 THz and 500 THz (660 nm, visible light), respectively, and (c) in case of the initial beam radius 15 mm with the same frequencies as (b).

in Fig. (c). It is here worth noting that the divergent of each beam and the difference among the frequencies with the 15 mm initial radius is much smaller. Fig. 2.8 indicates focus size as a function of the initial radius. As the radius change longer from 5 to 17.5 mm, or the frequency becomes higher from 0.2 to 3 THz, the focus spots become smaller. However, the focus size theoretically has a smaller limit even if with a larger initial size, depending on its wavelength and the aperture size of the lens. A series of measurements reproduces this trend, in case of the initial beam radius of 7.5 mm, shown in Fig. 2.9.
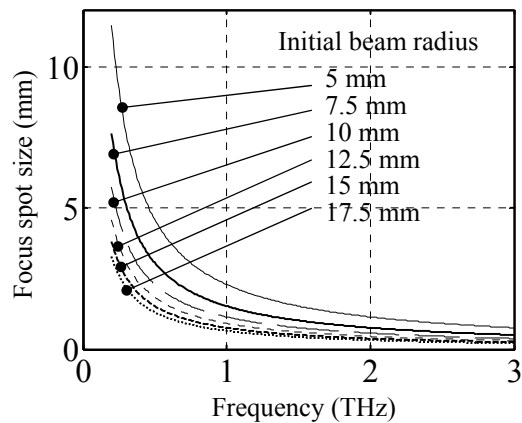
Focus spot size (mm)

Initial beam radius
5 mm
7.5 mm
10 mm
12.5 mm
15 mm
17.5 mm

Frequency (THz)

Figure 2.8. Focused radius as a function of the frequency, under initial beam radii of 5, 7.5, 10, 12.5, 15 and 17.5 mm.

-2   0   2
Distance (mm)

-2   0   2
Distance (mm)
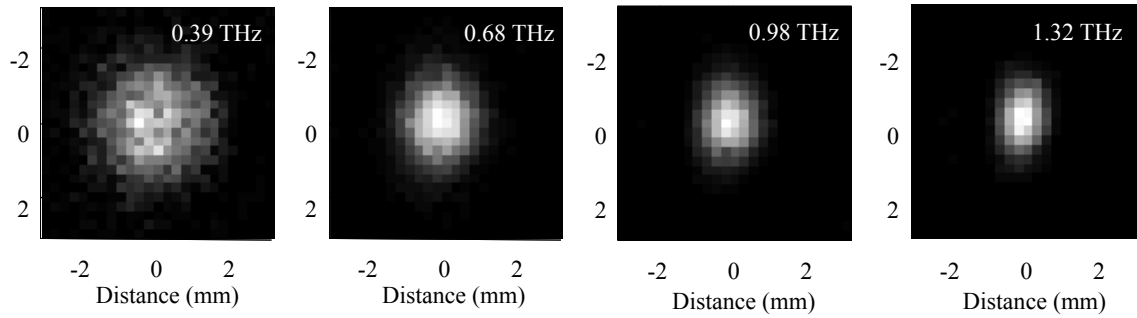
-2   0   2
Distance (mm)

-2   0   2
Distance (mm)

Figure 2.9. An example of measurements of the THz beam profile at the focal plane, S in the Fig. 2.7 (a). Each figure means at a frequency of (a) 0.39, (b) 0.68, (c) 0.98 and (d) 1.32 THz.

In case that the position of the lens L1 is out of the f configuration along the beam propagation, the focal position is also shifted away from the normal position. Especially, the THz wave shifts conspicuously as compared with the visible and the infrared light, because the range of the wavelength is remarkably wide. Fig. 2.10 shows a change of the focal position (Z') as the distance (Z) between the emitter E and the first lens L1 in Fig. 2.7 (a) is shifted ±60 mm from the center position (Z'=120 mm). There is a tendency that the distance Z' becomes shorter with smaller Z at any wavelengths. The dependence is slightly asymmetry and the amount of the change is larger as the frequency goes higher, e.g. 15 mm at 0.39 THz, 5 mm at 0.68 THz. The phase retardation between in the center and in the surrounding area isn't indeed so big, at the most, half-micron in Z=20mm and 4.5 μm in Z=60mm at 0.39 THz but it is required a condition that the offset of the distance Z from a 2-f configuration should not be more than few-cm order when the THz wave is applied to a measurement of surface profile with ten-micron order precision, such as a work in the chapter 4.
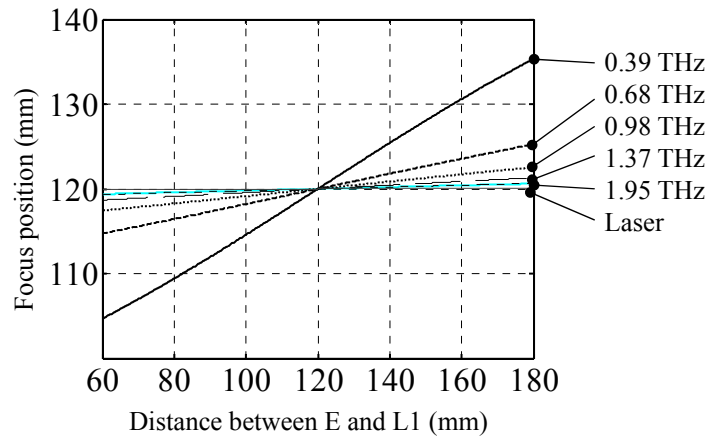

Figure 2.10. Shifts of the focus position as a function of the distance between the emitter E and the first lens L1 location.

- 11 -

3. Near-field radiation profile of large-aperture GaAs emitter

3.1. Background

The technique of time-domain THz spectroscopy is becoming increasingly important both in the field of research and in industry. Although several methods of THz generation have so far been implemented, special attention has been directed to biased large-aperture antennas, due to their unique carrier dynamics. It is known that large laser fluences result in strong saturation, the degree of which depends on such conditions as the illuminated area, the laser repetition frequency, the bias field, and the emitter material (typically GaAs, InP, or LT-GaAs). These aspects are dealt with in several publications [7, 55-64], while others focus on the propagation of the generated radiation [42, 65, 66]. In these, two types of screening effects were assumed – THz self-screening and electrostatic screening – which can explain the time-dependence of the total THz field along with the saturation of its total power [55,58,59,68].

Few papers, however, discuss the way saturation affects the spatial radiation pattern [67]. The exact field distribution is critical in such applications as THz radar, stated in the Chapter 4, or biological spectroscopy using dark-field imaging techniques [26, 69]. For this reason, I investigate the relationship between the spatial distribution of THz radiation and the optical pump power, where I show the presence of factors additional to the ones mentioned above, with which to fit my experimental data.

3.2. Theoretical model

A schematic figure of a photoexcited emitter with an applied bias V_b is shown in Fig. 3.1. The emitter is illuminated at normal incidence. For modelling purposes, the system is idealized to extend infinitely in the y-direction, so that all quantities are one-dimensional in the x-direction. The diagram depicts the relevant fields: the bias electric field E_b; the time-dependent inward and outward radiation electric and magnetic fields $E_{in}(t)$, $E_{out}(t)$, $H_{in}(t)$, and $H_{out}(t)$, respectively. It also shows the time-varying surface current $J_s(t)$. The boundary condition on the electric and magnetic fields, derived from Faraday's law, leads the surface current $J_s(t)$ to be represented as a function of the inward radiated electric field $E_{in}(t)$ [55],
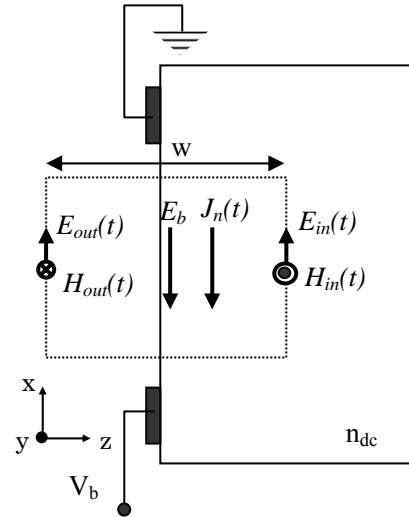

Figure 3.1. Schematic figure of a large-aperture photo-conducting antenna excited at normal incidence and biased with a voltage V_b.

$$J_{n,p}(t) = -\frac{1+n_{dc}}{\eta_0} E_{in}(t) , \qquad (3\text{-}1)$$

where n_{dc} is the index of refraction at THz frequencies and η_0 is the impedance of free space (377 Ω). From this equation and Ohm's law, the inward radiated field $E_{in}(t)$ at the emitter for electrons can be expressed as

$$E_{in}(t) = -E_b \frac{e\mu_n n(x,t)\eta_0}{e\mu_n n(x,t)\eta_0 + (1+n_{dc})} \qquad (3\text{-}2)$$

where $\mu_{n,p}$ is the electron and hole mobility. The total electric field is expressed by $E(x,t)=E_b(x)+E_{in}(x,t)$, therefore the radiated field is predicted to saturate. I note that these equations (3-1) and (3-2) are only valid for small variations of the electric field over the distance of a radiated wavelength.

Next, an inhomogeneous initial bias field $E_b(x)$ across the electrode gap was calculated using the finite element method. The electrostatic screening field in the plane of the emitter is given by

$$E_{in}(x,t) = \frac{e}{\varepsilon_s} \int \frac{\rho_p(x',t) - \rho_n(x',t)}{x'-x} dx' , \qquad (3\text{-}3)$$

to be evaluated in the principal value sense. Here ε_s is the dielectric constant of the semiconductor, and ρ_p and ρ_n are positive and negative sheet charge densities, respectively.

Finally, the continuity equations for electrons and holes are given by:

$$\frac{\partial n, p(x,t)}{\partial t} = \frac{I_{opt}(x,t)(1-R)}{h\nu} \pm \frac{1}{e}\frac{\partial J_{n,p}(x,t)}{\partial x} , \qquad (3\text{-}4)$$

where R is the reflectance, e the electric charge, $h\nu$ is the photon energy, and, $I_{opt}(x,t)$ is the incident optical intensity, taken as Gaussian in space and time with FWHM of 7.5 mm and 150 fs, respectively [68].

I numerically integrated Eqs. (3-1)-(3-4) in time, with boundary conditions $J = 0$ at the electrodes, to obtain the surface current $J(x,t)$. This boundary condition was chosen under a reasonable assumption that the external circuit is slow enough not to have time to recharge on the time scale of terahertz generation. From this, the Hertzian dipole result gives the far-field radiation pattern as

$$E_{THz}(x,t) \propto \frac{\partial J(x,t)}{\partial t} . \qquad (3\text{-}5)$$

These simulations were performed with and without an initial charge distribution.

3.3. Experimental setup and results

A schematic of the experimental setup is shown in Fig. 3.2. The laser was a Clark CPA 2001 Ti:Sapphire amplifier system, which supplied pulses of 150 fs duration at a wavelength of 775 nm and a repetition rate of 1 kHz. The pump beam was expanded by a telescope to 15 mm diameter and was directed onto a large-aperture GaAs emitter. The pulse energy was adjustable from 16 to 160 µJ with a rotation filter. The emitter measured 20x30 mm and was biased to 1 kV/cm. For measuring the spatial pattern of the generated THz beam, a metal plate with a 5 mm aperture was placed at a distance of 1 cm behind the emitter. The aperture was scanned in 1.0 mm steps in the plane transverse to the THz beam. Detection was done with a 1-mm-thick ZnTe electro-optic crystal [71]. The laser spot size was chosen as less than half the distance between the electrodes, as it was intended as the emitter of a THz radar system.
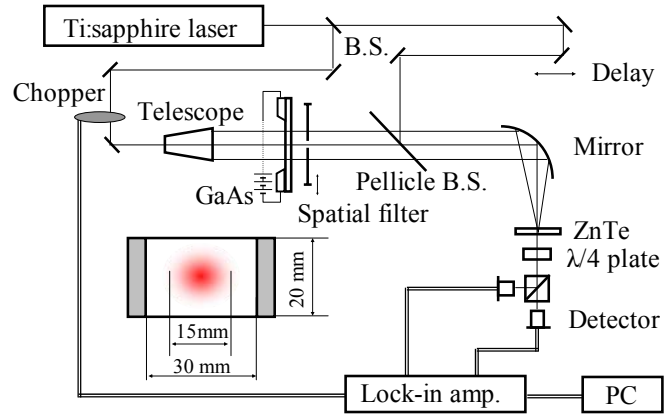
Fig. 3.3 shows a measurement series of the THz power component at 0.59 THz, measured at different pump powers. As can be seen in the insets (a) and (b), the power profile at lower

Figure 3.2. Experimental setup.
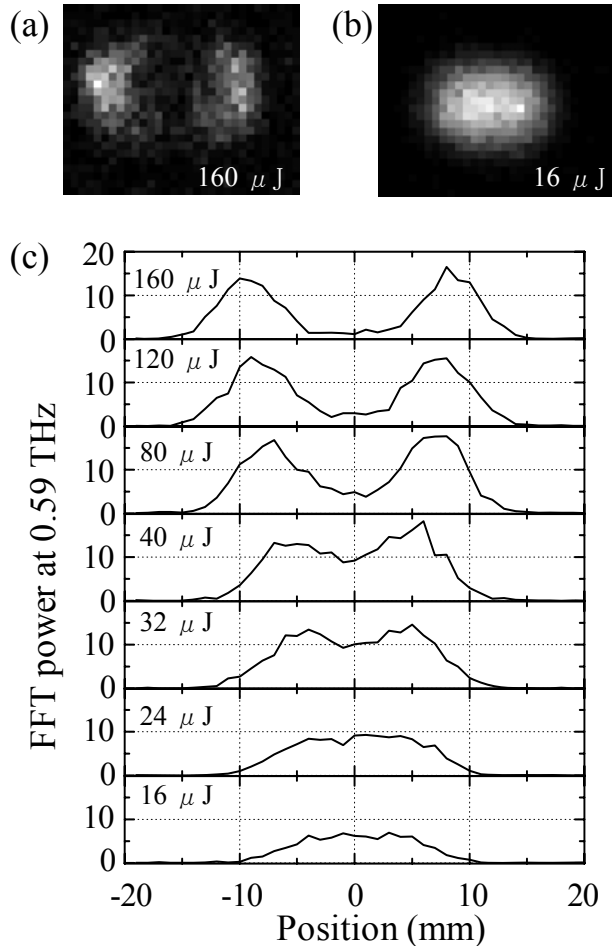

Figure 3.3. Measurement data of THz radiation pattern at (a) 160 µJ and (b) 16 µJ excitation power, in a spatial resolution of 1.0*1.0 mm, (c) FFT power signal at 0.59 THz along electrodes direction at 16 – 160 µJ.

excitation levels has only a single peak, while at higher excitation, two peaks clearly appear. Besides, the radiation pattern at 160 μJ is 1.5 times wider than 16 μJ. The general oval shape of the profiles is known to result from the shape of the CPA beam spot.

In (c) is shown the remarkable dependence of the radiation pattern on input fluence. As the fluence increases, one peak divides into two, and these maxima increasingly shift outward towards the electrodes. In addition, the radiated power at the center position shows an increase between fluences of 16 and 40 μJ, after which it shows a drastic decrease. In the figure only the power component at 0.59 THz is shown, but no qualitative difference exists for other frequencies.

Fig. 3.4 shows an example of time-domain data taken from the center of the emitter. The waveforms in Fig. 3.4 (a) display oscillations due to water vapor, but additionally, the curve for 16 μJ shows the typical small undershooting around 0.5 ps. This pulse has a width of 0.5 ps, corresponding to a spectrum ranging from 0.2 to 1.2 THz. As in Fig. 3.3, the emitted power has a peak at a fluence of 40 μJ, and higher fluence reduces this power. The normalized data of Fig. 3.4 (b) suggest the following two points: Firstly, the tailing feature of the pulses, between 0.5 and 1 ps, rises in proportion to the fluence, and is definitely positive at values above 80 μJ. Secondly, the peak position moves to slightly later times as the laser fluence increases.
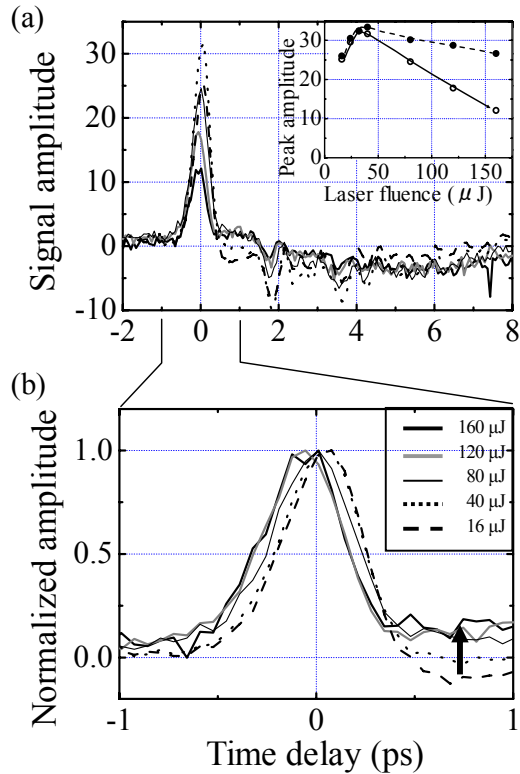

Figure 3.4. (a) Measurement data of THz radiation in time domain in the middle of the electrodes, with 16, 40, 80, 120 and 160 μ J excitation power. Inset: Laser power dependence of peak amplitude (hollow circles) and total output power (filled circles). (b) Normalized data, corresponding to the excitation power of (a).

3.4. Consideration and discussion

In this section I will compare two model scenarios. In the first, there are only two types of screening – radiation self-screening and instantaneous electrostatic screening -

while in the second I add residual carrier screening with ns to ms time scales. This will be shown to agree with the experimental results.

3.4.1. Spatial distribution of THz radiation

Fig. 3.5 shows the result of integrating equation (3-1)-(3-4), for the case without, and with initial carrier distributions. The y-axis represents the power component at 0.59 THz and is in arbitrary units. One may see that without initial carriers (dotted line), no double-peak structure appears at the experimentally used fluences. Only at fluences above 300 μJ does such a structure emerge. Moreover, only saturation is observed in the middle of the emitter, and never a reduction, as is experimentally observed. In addition, the emitted power extends all the way to the electrodes, although the laser spot is smaller than their distance. The sharp bend at 12.5 mm results from a combination of shading by the electrodes and the 5 mm aperture. These results are essentially those published previously [67], but do not approximate the experimental situation.

By contrast, the calculation which assumes an initial carrier distribution shows a remarkable signature and basically reproduces the experimental data. There is a clear transition from a single- to double peak shape, along with a maximum at the center at around 40 μJ. This shows that although the assumed residual carriers are so few compared with those induced by the laser pulse, the

Figure 3.5. Calculated FFT power of THz radiation at 16 − 160 μJ, with (solid lines) and without (dashed lines) initial carrier distribution and at 480 μJ, without initial carrier (the upper figure).

screening effect in the middle of the emitter is quite large. However, at higher powers the output power is inverted around the electrodes. This is a result of the fact that the electric field increases at the 10 mm position due to the field screening in the center of
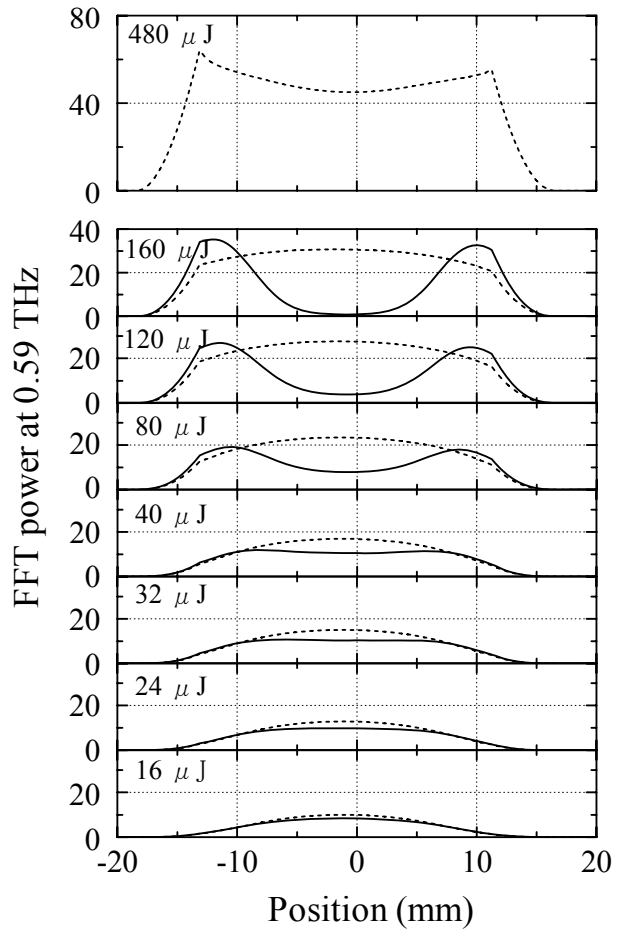
the emitter. Although there is a difference of relative output power between theoretical calculations and experiment, I suppose that this is caused by initial carrier distribution or the contact resistance between the electrodes and the photoconductor.

3.4.2. Time dependent behavior

Fig. 3.6 indicates calculated time-domain waveforms at the center of the emitter, corresponding to experimental data shown in Fig. 3.5. These waveforms display a slight asymmetry based on their generation of carrier excitation with subsequent relaxation to equilibrium. In the case without initial carriers, the pulse peak amplitude at each power indicates only saturation behavior up to 160 μJ, but never a reduction, similar to the simulation of the spatial distribution. On the other hand, including initial carriers, the dependence on laser fluence peaks around 40 μJ and is drastically reduced at more than 100 μJ, similar to the experimental data. This shows that the residual carriers proportional to laser fluence lead to a nonlinear THz response to the laser intensity.

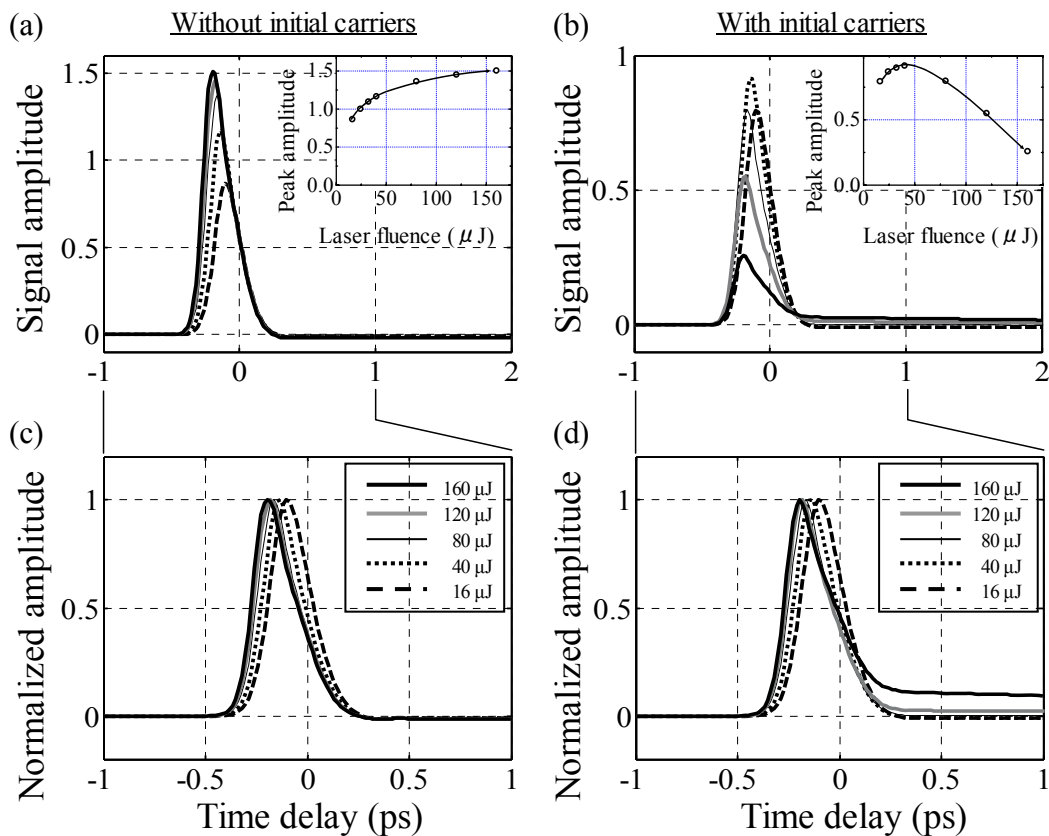
Figure 3.6. Calculated time domain data of THz radiation at five kinds of excitation power, 16, 40, 80, 120 and 160 μJ, (a) without and (b) with initial carrier distribution. Inset: Laser power dependence of peak amplitude. Normalized time domain data (c) with and (d) without initial carrier distribution.

3.4.3. Tailing feature

The normalized simulated waveforms are shown in the lower half of Fig. 3.6. In both cases the THz peak position shifts around 0.1 ps to earlier times of the range of excitation fluences. This feature is consistent with earlier publications [72], as well as my experimental data (see Fig. 3.7). The actual pulse shapes, illustrated in the top half of the plot, are markedly different. Without initial carriers, shown in Fig. 3.6 (a), there is no noticeable difference in each pulse
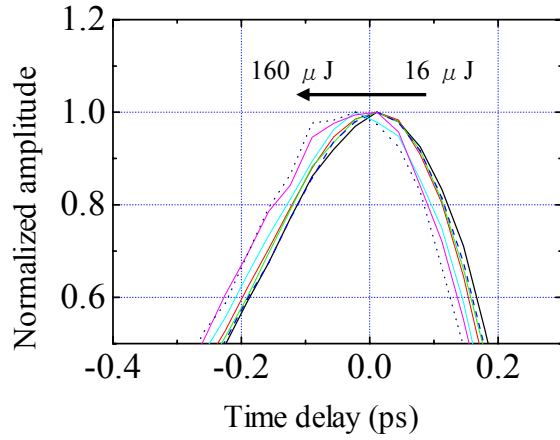

Figure 3.7. Experimental data zoomed in the time shift of THz peak position, with laser fluence 16, 24, 32, 40, 80, 120 and 160 μJ.

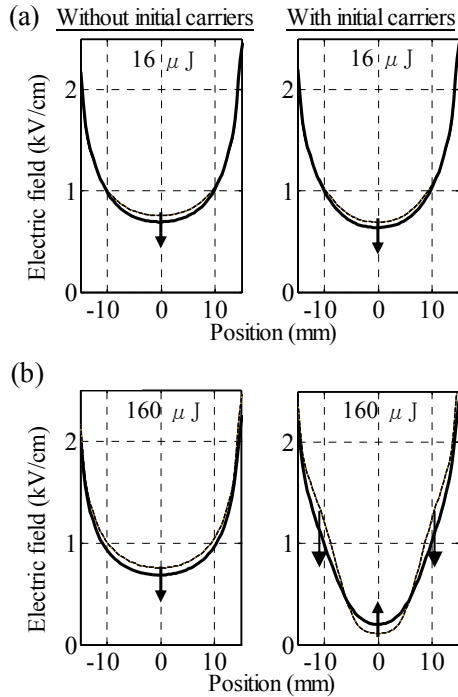Figure 3.8. Calculated electric field without (left side) and with (right side) initial carrier at 16 μJ excitation power, without (left) and with (right) initial carrier at 160 μJ. In all figures, dashed lines indicate initial condition and solid line 2 ps after laser pulse.

shape. All display a slight undershooting in the region around 0.2 ps. By contrast, with initial carriers included, the pulse shapes at lower laser fluence are similar to those without initial carriers, but at higher excitation, the signal remains positive, a feature which matches that of Fig. 3.4. This feature indicates that the current is still increasing after 0.5 ps, and that this phenomenon strongly depends on a screening effect of the electric field. Fig. 3.8 shows the initial electric field, and that 2 ps after carrier excitation. As can be seen in Fig. 3.8 (a), at low excitation there is no marked difference between the electric fields with or without initial carriers. After 2 ps, it is evident that the electric field in the center position is reduced by THz radiation and carrier screening. In the case of high excitation, however, an initial carrier distribution produces a remarkable change in that the electric field is increased

within 2 ps by a combination of screening effects by the initial carriers and those excited by the pump pulse. As a result, the surface current at the center increases only with the initial carriers and high excitation power. This is in contrast to the case of no initial carriers, where the electric field decreases after the laser pulse arrives. The tailing feature of the THz pulse in both experimental and simulated data is supported by this examination.

Finally, I note that the tailing behavior is independent of the THz pulse shape, which is affected by additional conditions such as laser and detector type, along with alignment. The pulse widths in Fig. 3.4 and 3.6 differ by a factor of 2.5. I suppose that the laser pulse is in fact slower-rising than the Gaussian pulse assumed in the calculation.

3.4.4. Discussion

In order to explain the experimental data, an additional screening mechanism needs to be assumed, since the saturation is very large and is impossible to fit with two screening effects already known. An initial carrier distribution must be assumed with the following two features: 1) the initial carrier density is proportional to laser fluence, 2) the carriers are concentrated around the electrodes (see Fig. 3.9 (a)). I believe that this kind of carrier distribution is a result of trapping of carriers from a previous pulse at a 1 kHz repetition rate, or from a small pulse which arrives 10 ns in advance of the pump pulse and which is called satellite pulses (see Fig. 3.9 (b)) [70]. In any cases, the calculation result implies that such a large saturation effect of the THz signal can be brought about by a small value of the carrier density, on the order of 10^{-6} of the total
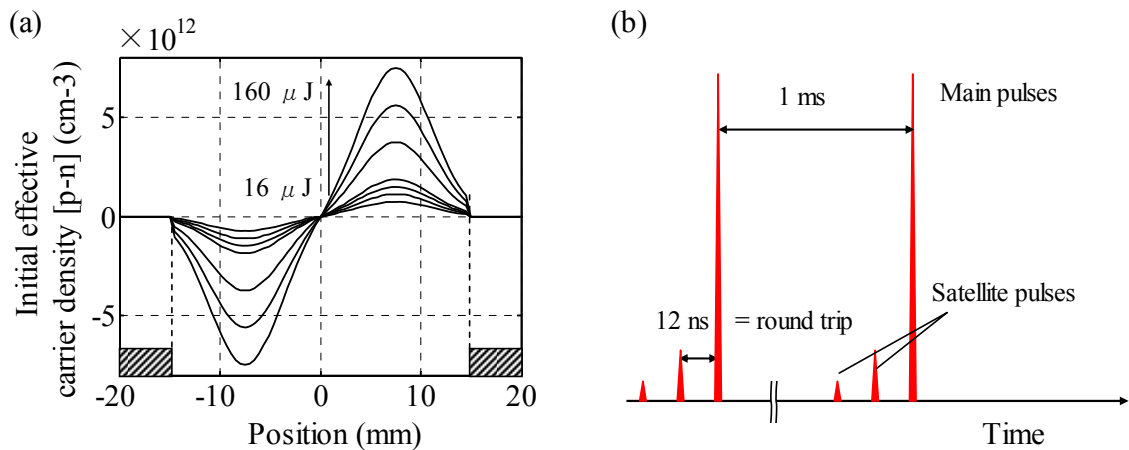

Figure 3.9. (a) Spatial distribution of calculated initial carriers at $16 - 160$ μJ excitation power and (b) relation between the main and the satellite pulses in the pulse train.

carriers excited by the pump pulse. This can be well explained with a small pulse (10^{-3} times the pump pulse) arriving 10 ns before the main pulse, together with an electron-hole recombination time of 5 ns

Finally, a simple simulation result, based on propagation theory of electromagnetic waves, is shown in Fig. 3.10. The THz radiation pattern from an emitter is shown in (a), while (b) shows the THz profile at the focus of a 120 mm lens. In the case of a Gaussian beam (dotted lines), the focus is also Gaussian. If the radiation pattern has a large hole in its center, the resulting focus shows has a roughly 20 % smaller spot size, with side lobes containing 15 % of the peak intensity. These differences are not as striking as those in the pattern of the radiation.

Figure 3.10. Calculated data of THz radiation pattern at (a) emitter and (b) focus position.

3.5. Conclusion

I have demonstrated that an absolute reduction in the emitted THz radiation at the center of a biased large-area GaAs emitter can occur, and can be modelled theoretically. This phenomenon can not be explained with familiar instantaneous screening effects, but a small residual concentration of carriers, 10^{-6} times the initial carriers, can such a large reduction in the emitted THz radiation. This assumption can explain both the spatial and temporal shape of the experimental data.
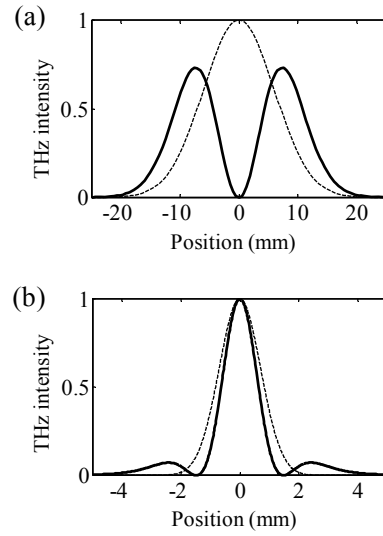
4. Radar application

4.1. Motivations

For more competitive product control in steel-making processes, it is under the necessity to detect and classify smaller surface structures, in the process of production. These typically have a millimeter-scale width and a height (or depth) between ten-μm-order and sub-millimeter. Contrary to the tiny sizes, a reliable detection is required to occur under specific conditions which include such aspects as a background surface roughness to the visible light, a large working distance of at least 10 cm. These conditions make it difficult to apply precise optical methods, like a microscopy or an AFM, to this purpose. From this background, CCD camera detections with incoherent white light or optical leverages using a 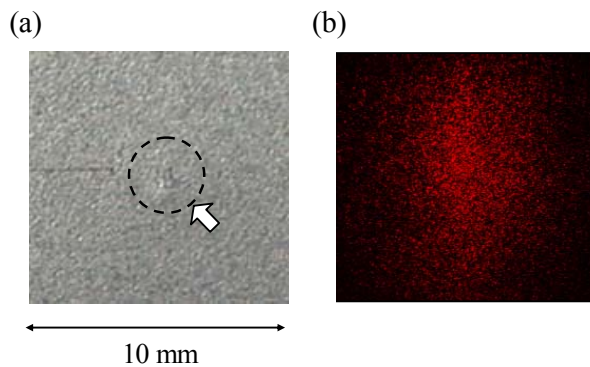laser beam have been employed. However, a factor (especially surface roughness) has brought optical methods a limit that structures consisting of gentle slope, such as protrusions and dents are undetectable, while they are placed among important objects, necessary to detect. As you can see Fig. 4.1, the CCD image (a) gives less contrast and the reflected scatter-like pattern (b) of a visible laser, includes much speckle noise,

(a)　　　　　　　　(b)

10 mm

Figure 4.1. (a) CCD image and (b) reflection pattern of He-Ne laser beam of a sample with a 2-mm-wide, 30-μm-high convex protrusion.

with a sample of a 2-mm-wide and 30-μm- high dent. The context has enough reasons to promote one searching for techniques which allow the online inspection, i.e., fast detection of and distinction among such kinds of surface structures. On the other hand, the THz technique provides advantageous features that the wavelength (300 μm at 1 THz in free space) can realize both to eliminate the influence of a rough surface and to measure in a ten-μm-order resolution with much lift-off, in principle.

4.2. Starting point

An imaging and a sensing with a free-space terahertz (THz) radiation [73] are promising approaches for the remote scanning of surface textures. Quite a few efforts have been devoted to the characterization and optimization of the depth resolution of pixel-by-pixel measurements. Because of the relatively longer wavelength of the radiation (300 μm at 1 THz in free space) compared to the visible range, reaching a depth resolution on the micrometer scale poses a certain challenge. A number of papers

have addressed this question and found that a resolution on the order of 10 μm can be achieved with the standard THz optoelectronic sources by applying such means as a polarization modulation [74], a time-of-flight measurements [75], and an interferometry [76, 77].

While these THz techniques allow to sensitively measure height variations on surfaces which consist mainly of planar segments, they are much less well suited to investigate the surfaces with non-planar topographical elements. In addition, it is worth noting that a conventional THz detection with a 2-f configuration enables one to recognize only negligible signal changes related to non-planar profiles on surfaces (see Fig. 4.2). Their detection and rapid classification, however, is often desirable, and calls for the development of dedicated measurement techniques.
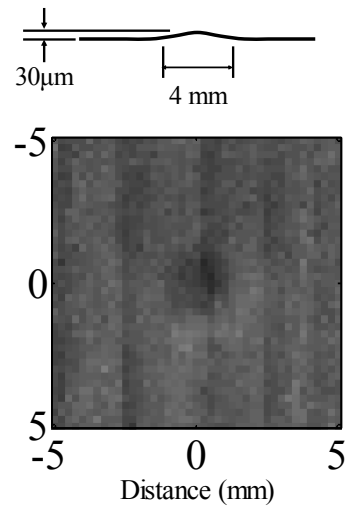

Figure 4.2. Detected images of a non- planar convex shape with 30 μm height and 4 mm width by a conventional THz measurement with 2-f optical configu-ration.

4.3. Background
4.3.1. Dark-field technique

A concept of the dark-field comes from an imaging technique, generally used in a field of an optical microscope or a TEM. A simple example of the dark-field microscope is schematically illustrated in Fig. 4.3 (a). The point is that an object is illuminated at a low angle while an objective lens is established perpendicularly to the object surface. A ring-light-source is often employed to obtain the low angle illumination for canceling
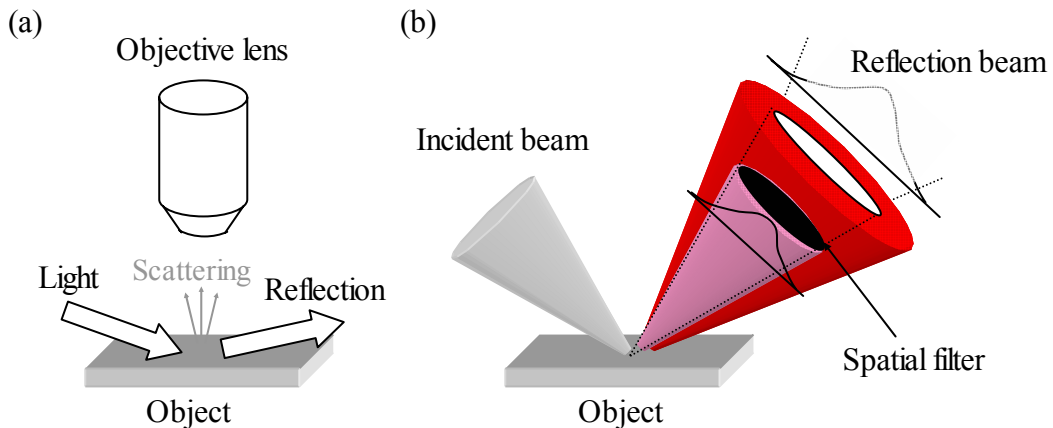

Figure 4.3. Conceptual illustration of (a) a dark-field microscope and (b) a dark-field detection of THz beam.

direction dependence, but it is no difference in principle. If the object surface is perfectly flat, the lens receives no reflected light. In case there is a scattering element on the surface or what leads to change of the reflection direction, some parts of the reflected light goes through the lens. At this time, the element is observed as a bright image in the completely dark background. This is the origin of the so-called "dark-field" and it makes possible to detect a small scattering element with high sensitivity.

A THz dark-field technique has the same basic idea in a point of selectively detecting the scattered light, while it is defined as a broader sense, in that an observed image is not necessary in a dark background and that an element which causes diffraction, as well as the scattering, is clearly included as the objects. The scattered or the diffracted component is generally propagated along a different direction from the exact reflection. If a spatial filter screens some amount of the reflected THz beam, as shown in Fig. 4.3 (b), the transmitted beam should hold relatively much scattered or diffraction component. This brings to emphasize a signal change caused by surface undulations. Besides, it leads to determine the structure of the objects, because it is thought that the spatial pattern of these components reflects its character on the surface.

4.3.2. Propagation model

The model based on a paraxial Helmholtz description of the beam propagation is schematically illustrated in Fig. 4.4. Each THz component is entirely arranged in a 2-f configuration that the distances between lenses and the other components are equal to the focal length f (120 mm) of the lenses, adjusting to a below experimental setup. This formation actually ensures that each frequency component of a THz pulse has the same focal position, as mentioned in Chapter 2.3. I choose the center position between the two lenses (Fourier plane) as a spatial filter location, because all THz frequency components have the same spot size here. Additionally, the lenses also could be replaced to a paraboloidal mirror, having the same off-axis distance.
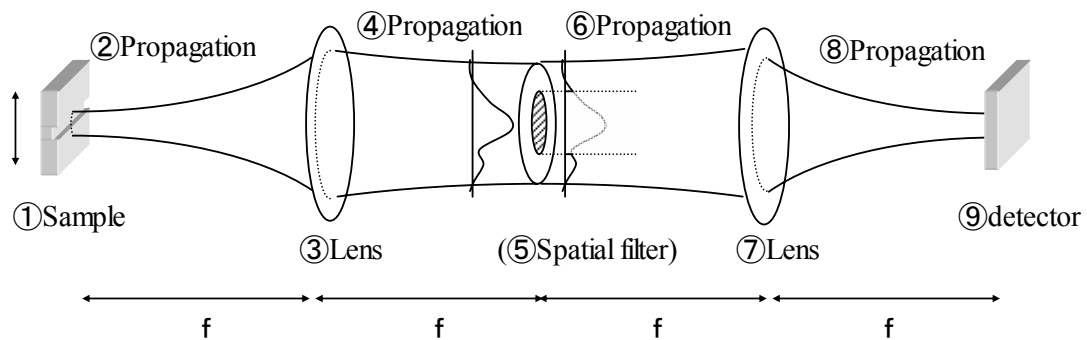

Figure 4.4. Optical formation in the propagation mode.

The electric field $E_0(x, y)$ (x, y denoting coordinates perpendicular to the beam axis) directly behind the sample is given by [78]

$$E_0(x, y) = \exp\left(-\frac{x^2 + y^2}{w_0^2}\right) \cdot M_I^{1/2}(x, y) \cdot \exp\left[i\{\varphi + M_\varphi(x, y)\}\right], \quad (4\text{-}1)$$

where w_0 is the focus diameter of the THz beam on the sample, and φ is an initial phase factor set equal to zero here. The intensity and the phase modulation functions, represented by $M_I(x, y)$ and $M_\varphi(x, y)$ respectively, are set equal to one and zero when a sample with a flat surface is applied. It is here important to note that this modulation represented by the sample features can easily switch a condition of transmission into of reflection. In case of transmission (reflection), the incidental beam is assumed to illuminate from back (top) side. There is only a difference that the sample height (depth) in the reflection calculation must be increased double as much as the actual value.

After taking off the surface, the THz beam propagates according to the following equation, induced from a paraxial diffraction theory;

$$E_z(x, y) = \frac{1}{j\lambda z} P_z(x, y) \int_{-\infty}^{\infty} \int_{-\infty}^{\infty} \{E_0(x_0, y_0) \cdot P_z(x_0, y_0)\} \exp\left[-j2\pi\left(\frac{xx_0 + yy_0}{z\lambda}\right)\right] dx_0 dy_0, \quad (4\text{-}2)$$

where, $P_z(x, y) = \exp\left[\frac{jk}{2z}(x^2 + y^2)\right]$ is a phase factor with unit modulus. And, under an assumption of a thin lens system, the electric field is converted by the equation, if f is the focal length of it;

$$E_{z'}(x, y) = E_z(x, y) \cdot \exp\left[\frac{jk}{2f}(x^2 + y^2)\right]. \quad (4\text{-}3)$$

The detected electric field is calculated by integrating the electric field at the detector position over a central area with a diameter of 0.5 mm corresponding to the region which in the experiments is interrogated electro-optically by the optical probe beam. The detected field is expressed by

$$E_{z'}(x, y) = \sqrt{\frac{1}{z\lambda}} \int\int_{area} E_z(x_2, y_2) dx_2 dy_2 . \quad (4\text{-}4)$$

In case of the dark-field measurements, a circle-shape beam stop is located in the middle of the two lenses, coincident with each center of the THz beam and the beam stop. Contrary to detection, the center part of the beam is filtered out.

Some examples of the calculations, on the assumption of with a sample of a 20-μ m-deep round-shaped protrusion, a slit, a groove with 50 μ m depth, made of metal, in the reflection configuration, and a 1-mm- thick bar (assuming the transmittance is 0.8) in the transmission configuration (all are 2-mm-width), respectively, are listed in Fig. 4.5. The upper column gives information on the sample structures, the intensity

and the phase modulation function as initial conditions (in the middle), and the beam intensity in the middle position of two lenses of Fig. 4.4 (in the bottom). A Gaussian function with a $1/e^2$ width of 1.84 mm is applied as an incident beam in all cases. I assumed the protrusion (a) in reflection configuration induces only the phase modulation. The calculation result predicts that the convex shape with a height of $20\,\mu$ m carries broader beam profile, even small, by changing the reflection path. In the same way of thinking, the slit shape (b) induces only the intensity factor, the groove (c) only the phase factor, and the bar shape (d) in the transmission configuration yields both an intensity reduction, according to the absorption and material thickness, and a phase delay by the refractive index and its thickness. The planar function in the last three shapes ((b)–(d)) is described by a super-Gaussian with a power of 10, avoidable aliasing problems. The calculation results concerning these samples including such a function yield clear diffraction signatures in common, but they give impressive features that each shape shows various patterns based on the initial condition. In this way, a combination of the intensity and the phase factor in the model makes it possible to describe several cases of the sample structures, provided of taking the phase modulation as an infinitely thin mask.
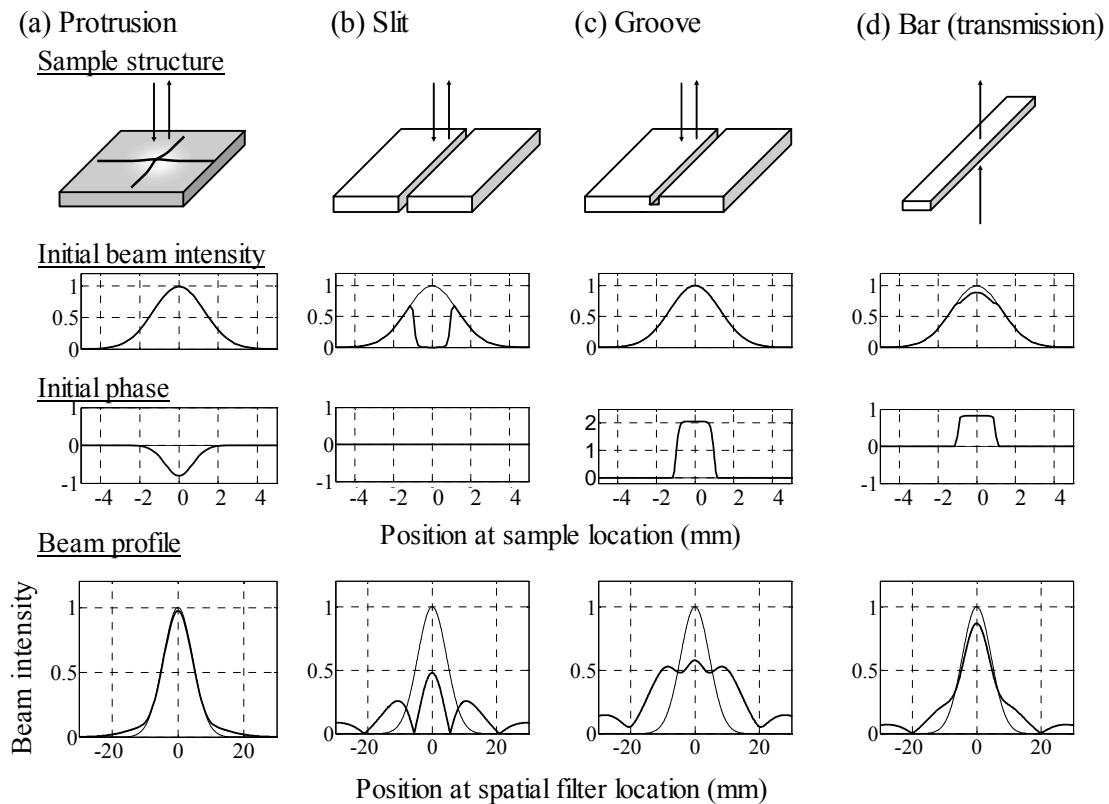

Figure 4.5. Sample structure (the upper column), initial intensity and phase condition (middle) and THz beam intensity (bottom) at the spatial filter position (see in the figure 4) by (a) a 20-μ m-high protrusion; (b) a slit; (c) a 50-μ m-high groove in a condition of reflection; and (d) 1-mm-thick bar in transmission configuration. In all cases, the thin lines indicate a condition of flat surface.

4.3.3. Signal processing flow

Before moving onto examples of actual experiments, I briefly mention the way how to process a detected signal. A time dependent electric field of a THz beam is experimentally detected in various relative positions between the THz focus and an element on a surface. The sample is actually moved in a small (like 0.25 mm) step, while here the left column in Fig. 4.6 indicates three examples of the sample configuration. When time domain data are measured, the detected signals may be varied at each position. As the offset goes larger, in this example, a component from the bottom becomes less and only the beam from the top is detected in the case (3), because this sample shape brings interference between the top and the bottom surfaces. After taking the Fourier transform, variations in the frequency domain are observed, if the signal exists. Then, the relation between the sample position and the FFT intensity is plotted, by sampling certain frequency components at each position. Please take note that the plot is normalized at the fixed frequency at the same time.
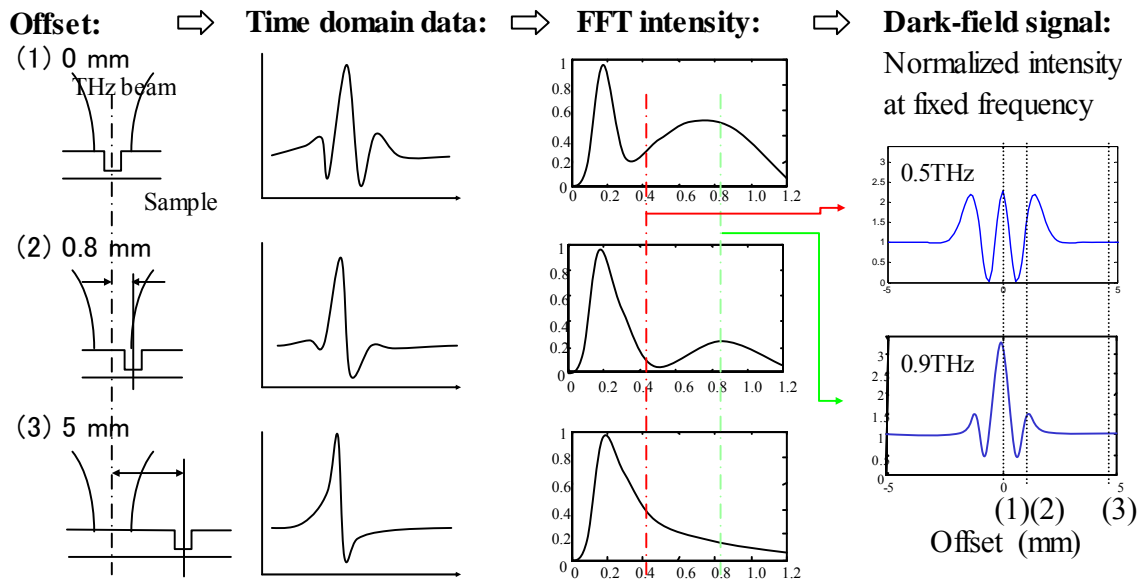

Figure 4.6. Signal processing flow.

4.4. Approach 1　- Dark-field technique -

The first approach which I propose to utilize is a THz dark-field technique. In this section, I have an intention to verify that THz waves are not affected by the optical surface roughness, and that this technique gives a possibility to detect and classify $5\text{-}\mu$ m to sub-millimeter sized structures on the surfaces through experimental and theoretical examinations.

4.4.1. Experiment and calculation results

Fig. 4.7 schematically illustrates the experimental setup (for details, see [26]). A Clark CPA 2001 Ti:sapphire amplifier laser system supplies pump and probe laser pulses of 150 fs duration at a wavelength of 775 nm and a repetition rate of 1 kHz. The pump beam is expanded to 25 mm diameter by a telescope and illuminates a large-aperture GaAs THz emitter [55]. The generated THz pulses are then focused onto the sample, the focal spot size being approximately 3 mm (at 1 THz). The reflected, or alternatively, transmitted signal is passed through a dark-field spatial filter (containing a beam stop of 10-mm diameter) and detected electro-optically with a 1-mm-thick ZnTe crystal [71].

The setup includes two THz beam configurations, one for detection in transmission (indicated by the solid line in Fig. 4.7) and one for reflection (dashed line), with path selection via the insertion or removal of the flat mirror M1. In the transmission (reflection) geometry, the sample is inserted perpendicularly (under 45 degrees) to the THz beam. The position of the
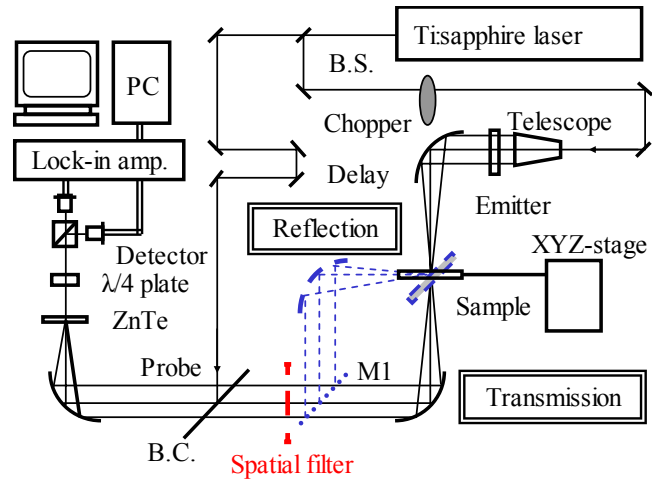

Figure 4.7. Experimental set-up for transmission measurements (solid line) with perpendicularly inserted sample and for reflection measurements (dotted line) with sample inserted at 45 degrees.

sample is manipulated by a computer-controlled XYZ-stage. It is important to note that the THz source and the sample are positioned in a 2-f geometry in order to ensure that each frequency component of the THz beam has its focal point on the sample. In addition (and in contrast to [26]), the first two paraboloidal mirrors have the same off–axis distance (i.e., effective focal length) of 120 mm, whilst the third mirror, which focuses the THz radiation into the detection crystal has an off-axis distance of 50 mm.

I first investigate a 2-mm-wide and 1-mm-thick rectangular bar made from THz-transparent TPX (chemical name: 4-methyl-1-pentene, the index of 1.46) in the transmission geometry. Experimental and theoretical line-scan data (step width: 0.25 mm) are shown in Fig. 4.8, for four different frequencies, 0.39, 0.68, 0.98 and 1.32 THz. The horizontal axis indicates the sample position, and the vertical axis the intensity of the THz signal at a certain frequency obtained by Fourier-transform of the time-domain data, plotted by hollow circles. The theoretical data (full thick lines) are calculated assuming the TPX sample is 1 mm thick, with a transmittance of 0.9. Qualitatively and

quantitatively, the calculations reproduce the experimental data very well. These data are dominated by an oscillatory feature typical for diffraction effects. Another theoretical data calculated under a condition of a normal detection without the spatial filter (full thin lines) clearly prove that the feature is enhanced by the dark-field geometry. As might be expected, the spatial period of these features decreases with decreasing the wavelength. However, from additional numerical investigations I observed that these oscillations and the relative proportion of constructive and destructive interference depend in general on the relative spot size and sample optical path length as well. In the present case, for instance, the net phase retardation of the TPX sample at 0.68 THz is approximately 2π, and hence the sample leads to only a very weak diffraction at this frequency. These data demonstrate that using a set of frequency-resolved data affords excellent sensitivity to both lateral and depth features. The signal-to-noise ratio at higher frequencies decreases because of the lower available spectral intensity in this range. The asymmetry of the signal measured at 1.32 THz presumably arises from an imperfect rotational symmetry of the THz beam (deviation from Gaussian beam shape).
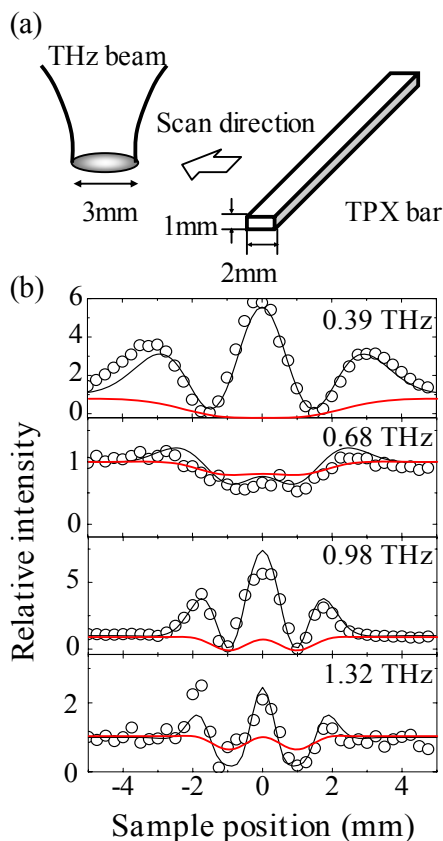

Figure 4.8. (a) Illustration of the geometrical proportions of the THz beam focus and the TPX bar sample; (b) experimental data (dotted circles) and calculation results of the 2-mm-wide and 1-mm-thick TPX bar, with (black full lines) and without (red full lines) a spatial filter at four frequencies in transmission geometry.

Fig. 4.9 shows measured signal patterns of two sheet-metal samples measured in reflection geometry. Fig. 4.9 (a) refers to a 5-mm-thick polished brass plate containing a 2-mm-wide slit. The data again exhibit clear diffraction signatures. Except for the slight asymmetry at high frequency mentioned already before, the theoretical data reproduce the experimental data extremely well.

Fig. 4.9 (b) displays line-scan data of a polished brass plate which contains a single circular protrusion of 30 μm height and 4 mm base width. The theoretical data reproduce the basic feature of the experimental data, but the agreement is not as good
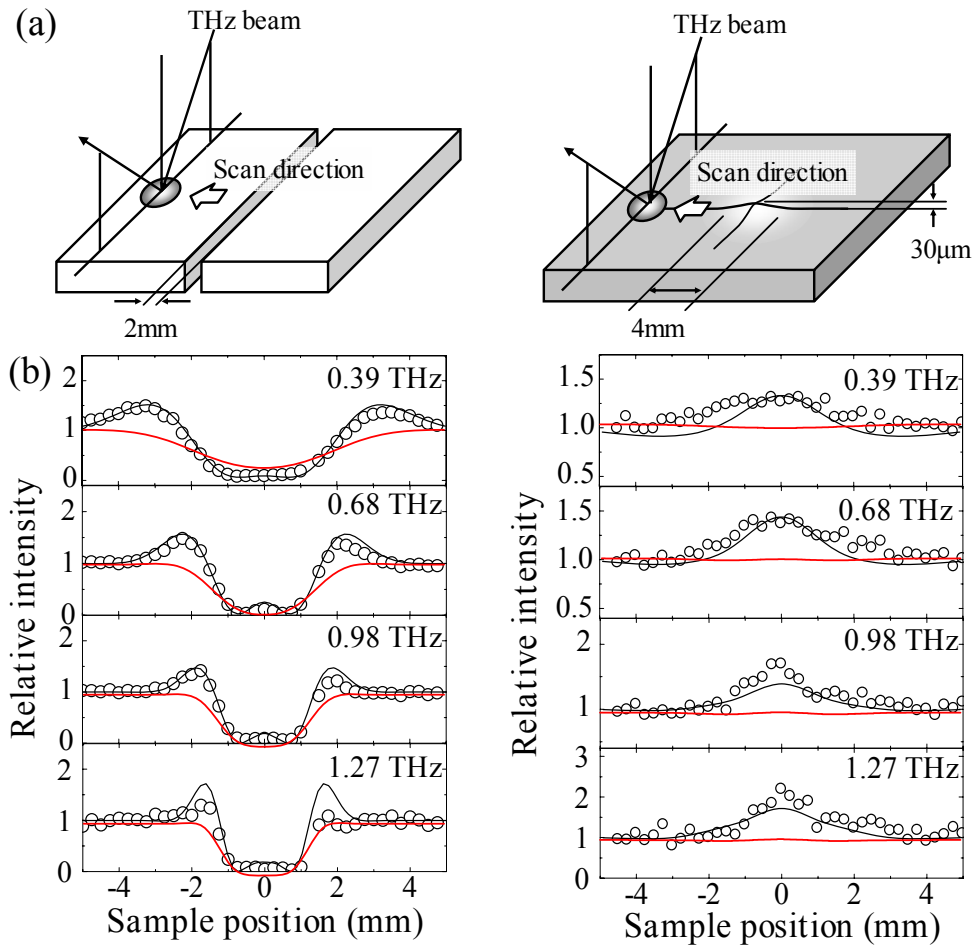
Figure 4.9. (a) Schematic illustration of polished-brass sample structures with smooth surfaces, 2-mm-wide slit (left side) and 4-mm-wide, 30-μm-high dent (right); (b) experimental data (circles) and calculation results of the slit (left) and dent (right) samples with (black full lines) and without (red full lines) a spatial filter at four frequencies in reflection geometry.

as for the slit sample. The difference results mainly from a lack of knowledge of the precise shape of the protrusion which is assumed in the calculations to be of Gaussian character. In addition, the modeling treats the protrusion as an infinitely thin phase retardation, so that spatial displacement and shadowing effects due to the finite height of the protrusion are neglected.

It is important to note that the signal patterns of the three samples are remarkably different from each other. This strongly suggests that it may be possible to employ THz radar patterns to classify surface profiles.

I will not pursue this potentially far-reaching aspect further here, but rather come to the question of the detectability of mm-sized surface features on optically rough metal surfaces.

Experimental data for two sheet-metal samples with rough surfaces, approximately

peak-to-peak 10 μ m, measured in reflection geometry, are shown in Fig. 4.10. One sample (left side) contains two grooves, a wider one of 0.5 mm width, and a narrower and very shallow one of 0.2 mm width. While the wider one gives a clear THz signal, the narrower one is not detected with radiation at 1.37 THz. Its detection will require tighter focusing and/or shorter wavelength.

The second sample (right side of Fig. 4.10) contains a protrusion of about the same size as in the case of the brass sample (Fig. 4.9). The protrusion is difficult to detect with conventional optical methods (see CCD image). In the THz image, however, this surface feature is located unambiguously.

It is worth noting that signal patterns in the line-scan data of both samples are similar to the corresponding THz dark-field data of optically smooth samples. This demonstrates that any feature recognition algorithm could be applied independently of the optical roughness of a set of samples.
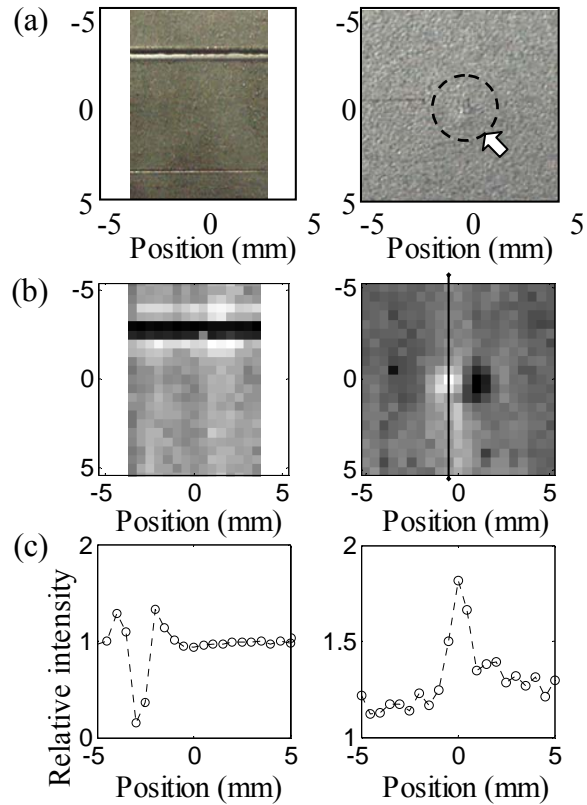
Figure 4.10. (a) CCD images of the measured samples with optically rough surfaces, one containing two grooves of 0.5-mm and 0.2-mm width, the other a convex dent of about the same size as the brass sample in Fig. 9; (b) THz images (0.5 mm * 0.5 mm/pixel), measured in reflection geometry, of the two samples at 1.37 THz (groove sample) and at 0.98 THz (convex dent); (c) corresponding THz line scans.

In this section, I have presented an analysis of the diffraction and scattering of the THz pulses at the surface structures. From a result of it, I have verified that the dark-field detection with 25 % intensity beam stop makes it possible to detect millimeter-sized samples with unique interference patterns, depending on the sample structures and that there is essentially no difference between the smooth and the rough surfaces, to the THz signal.

4.4.2. Optimization of the beam-stop size

I focus on a detection of a protrusion and a dent shapes with higher sensitivity, for they yield relatively a small signal change, even if its height is 30 μ m (target: 5 μ m).

Fig. 4.11 (a) gives an example of calculated signals in a variation of the beam stop size, for a sample with a 20-μm-height and 2-mm-width protrusion. But please take note that the THz focus conditions with a focused radius of 1.84 mm in 0.98 THz are slightly changed, corresponding to have been switched an emitter of GaAs into a non-linear crystal in the following experiments (the size employed in the experiments, stated in Section 4.3, is correspond to 10 mm diameter in this condition). Suppose I take notice of only the signal intensity, this result clearly indicates that a larger size drastically emphasize the signal intensity, from almost no signal without the beam stop to 3000 times larger with a 30-mm-diameter beam stop. The signal shape can also allow one to plot only the center peak intensity, in order to estimate the signal change related to the beam-stop size. Fig. 4.11 (b) shows relative signal intensity as a function of the beam stop size for variation of the object size. The intensity has certainly dependence, in a different ratio, on the object height and width that the higher or narrower shape yields more signal, while, its tendency evenly gives the same feature as a larger blocker
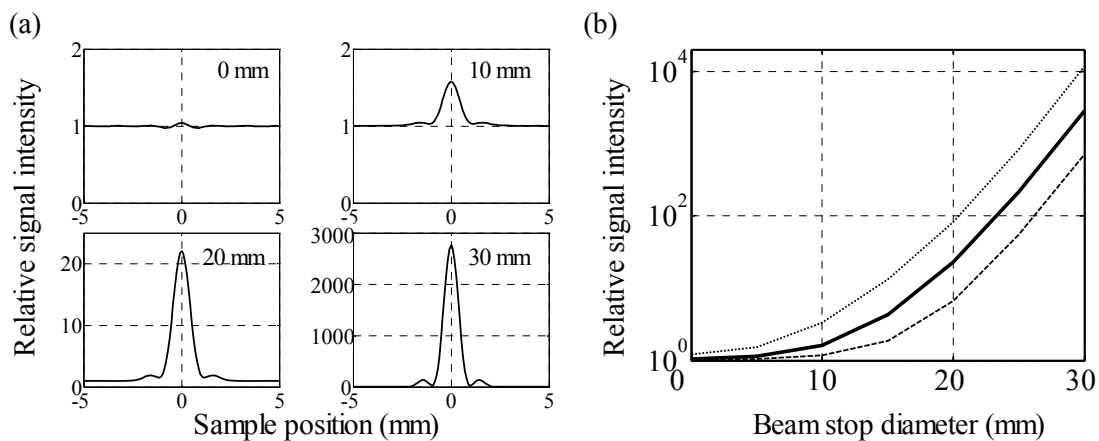

(a)

(b)

Figure 4.11. (a) Calculated signals of a 2-mm-wide, 20-μm-high protrusion without a spatial filter (0 mm), and with a beam stop size of 10, 20 and 30 mm; (b) relative signal intensity as a function of beam stop size, of a protrusion with 2-mm-width and 10-μm (short dotted line), 20-μm (thick full line), and 40-μm (dashed line) height (at a frequency of 0.98 THz).

provides a higher signal and that there is no sign of an optimum size. I thought, however, that there might be a limit, in reality, from the following two points of view.

The first point is the absolute value of the signal. Some calculation results in Fig. 4.12 indicate the relation between the detected signal intensity and the beam stop diameter in a few heights of the dents with 2-mm-width. Please take note that the vertical axis is plotted in a logarithmic scale. It is indeed true that the differential between the reference signal (thick-full line) and the signals with dents (height: 20 μm (thin-full line), 10 μm (dashed line) and 5 μm (dotted line)) becomes larger, as the beam stop
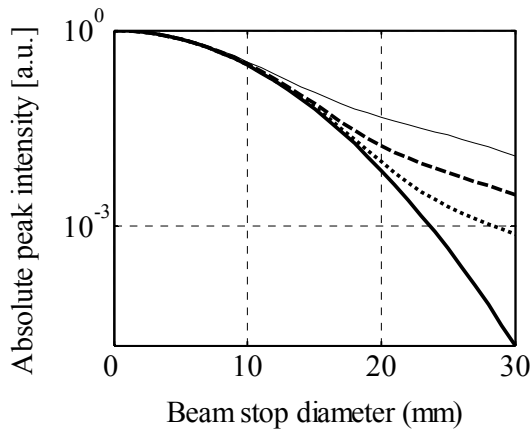
Figure 4.12. Absolute (without division by a reference) signal intensity as a function of beam stop size with 2-mm-wide, 5-μm (dotted line), 10-μm (dashed) and 20-μm-high (thin full line) protrusion, and flat surface (thick full line).

Figure 4.13. (a) Scheme of dark-field imaging. The coordinate x' denotes the line profile direction. (b) Results of model calculations: THz beam profile at the beam-stop plane for a 0.98-THz beam coming from a flat surface (full line) and the center of a dent (dashed line) with the same parameters as in Fig. 12. (c) Beam profile change of 2-mm-wide and 5-µm (dashed line), 10-µm (dotted line) and 20-µm (full line) high protrusion to reference from a flat surface, as a function of radius position at the beam stop location.

diameter increases, but each power goes down in an increasing rate. It may safely be said that the strong enhancement dominantly comes from rather reduction of the reference signal in a region of over 20 mm diameter. The percentage of the screened intensity, about 50 % with 10 mm, reaches 99.3 % with 20 mm, up to 99.99 % with 30 mm. It is generally hard to define the criteria in this case, but it is not entirely a failure to ensure signal intensity of more than $1\text{-}2*10^{-3}$ to the smallest dent, taking into account that the raw signal-to-noise ratio is 10^{-4} to 10^{-3} in actual measurements. Therefore, a diameter of more than 25 mm is not suitable to be applied.

Secondary, I direct my attention to the beam profile change in the Fourier plane. The full line of Fig. 4.13 (b) displays the cross-sectional beam profile of the assumed THz beam (frequency: 0.98 THz) at the beam-stop location (see Fig. 4.13 (a)). The dashed line represents the beam profile if the
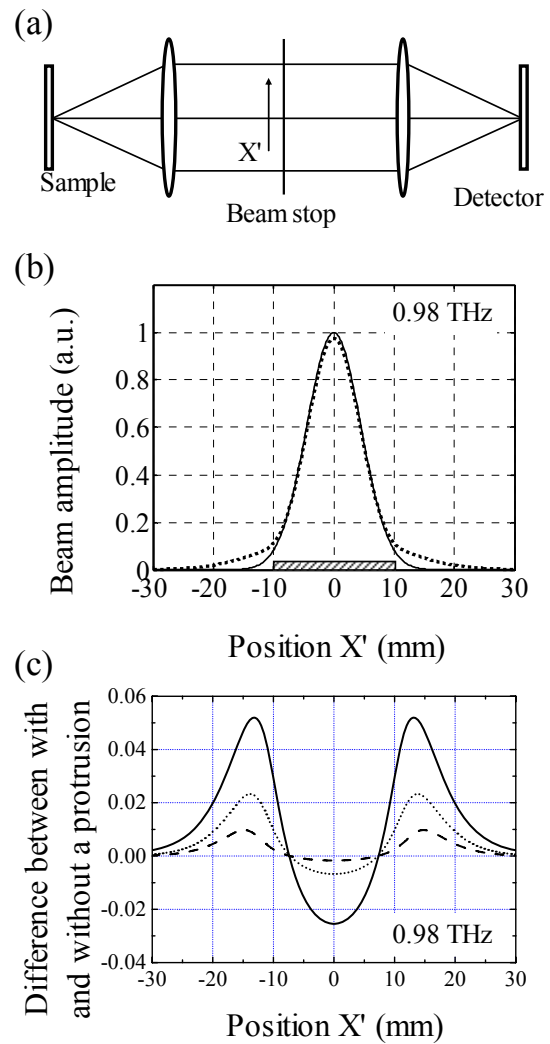
incoming beam impinges onto the center of the protrusion. While the middle part of the beam is weakened, the wings become more pronounced. The subtraction of the reference component from the signals with three kinds of protrusions in Fig. 4.13 (c) clearly shows this feature as well. It is important to note that the amplitude change of the outer profile is the most pronounced, positioned between 10 and 20 mm radius, in any cases. From a result of the consideration, I reach a decision that a beam-block diameter of 20 mm should be applied to experiments.

4.4.3. A problem of the spatial-filtering detection

The relative detected intensity (normalized to the small background signal from the flat surface) is plotted in Fig. 4.14, as a function of the sample position (x-coordinate) in case of that a 20 mm beam-stop is applied. For example, the 1.95 (0.98) THz signal shows a large relative intensity of 250 (23) when the protrusion is centered on the THz beam. Note that one expects only a negligible intensity change in such a 2-f configuration when no beam stop is present, as was experimentally verified (presented in the results of the below experiments in 4.5.2).
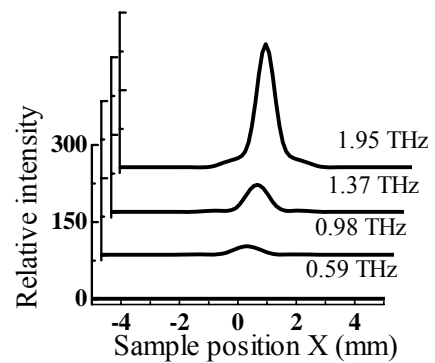
The expected relative intensity was calculated for a range of THz frequencies and shows that the signal is significantly enlarged at higher frequency.

Figure 4.14. Calculated normalized intensity of the detected signal as a function of the sample position for various frequency components.

This is a result of both the reduced focal spot size at higher frequency and the frequency-dependent phase shift of $M_\varphi(x, y)$ in Eq. (4-1) which strengthens the diffraction.

Performing calculations for a dent instead of a protrusion – which in the scalar approximation of Helmholtz theory is achieved by simply changing the sign of $M_\varphi(x, y)$ – results in the same detected intensity profile. Thus it is impossible to distinguish between complementary protrusions and dents using this experimental design.
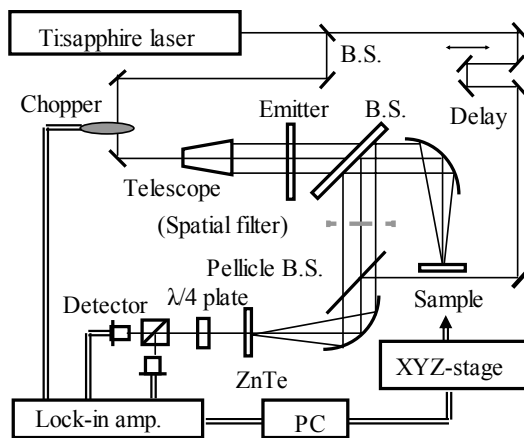

Figure 4.15. Experimental set-up. In the case of dark-field detection, a spatial filter (shown in light gray) is incorporated between the paraboloidal mirrors.

I experimentally verified the results of this model by measurements with a THz imaging system based on an Clark CPA 2001 Ti:sapphire amplifier laser system (see Fig. 4.15). The laser supplies pump and probe pulses of 150 fs duration at a wavelength of 775 nm and a repetition rate of 1 kHz. The pump beam is expanded by a telescope to a diameter of 20 mm and illuminates a ZnTe THz emitter [9, 26, 27]. After passing through a 5-mm-thick, highly resistive Si wafer, which functions as a 50:50 beam splitter, the generated THz pulses are focused onto the sample, the focal spot diameter being approximately 3.7 mm (at 1 THz). The reflected beam travels back along the path of the incoming beam and is coupled out by the Si beam splitter and refocused into the electro-optic detector (1-mm-thick ZnTe crystal [71]). For dark-field imaging, a spatial filter, which consists of a beam stop with a diameter of 20 mm and filters out almost the same amount of power as in the calculation, is inserted between the Si beam splitter and the pellicle beamsplitter (which serves to combine the optical probe and THz beams). The position of the sample is manipulated by a computer-controlled xyz-stage. It is important to note that the THz source, the sample, the spatial filter and the detector crystal are all positioned in a sequence of 2-f positions in order to ensure that each frequency component of the THz beam has its foci at the same points in the setup.

Figs. 4.16 (a) and (b) display measurement results obtained with polished copper samples which contain either a dent of 2-mm width and 20-μm height (left column), or a protrusion of 4-mm width and 30-μm height (right column), these parameters being determined by optical interference microscopy. The 0.98-THz images of Fig. 4.16 (a) represent single-scan data taken with a lock-in time constant of 50 ms, the pixel step size being 0.25 mm in both the x- and y-direction. The line-scan data of Fig. 4.16(b) display the
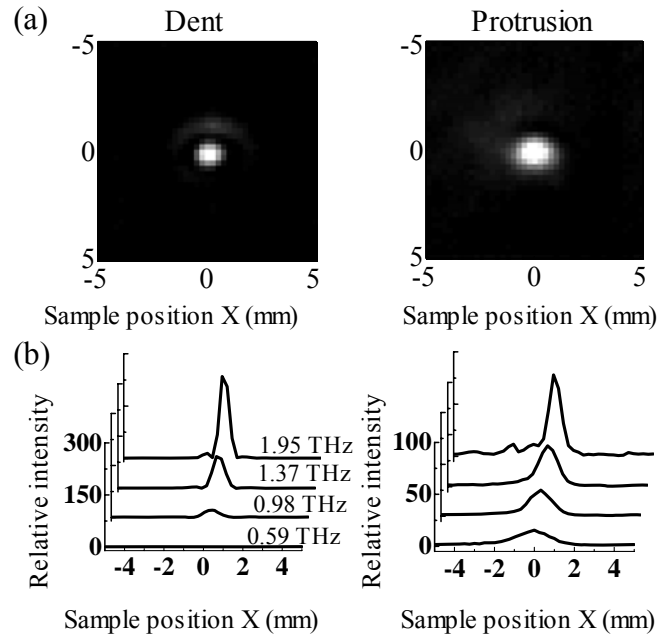

Figure 4.16. (a) Measured intensity profiles for reflection of the 0.98-THz Fourier component off a dent (left side) and off a protrusion (right side) as a function of sample position. (b) Line scans through the centers of Fig. 14 and corresponding profiles for various Fourier components.

cross-sectional intensity profiles for various Fourier components of the signal.

The predictions of the calculations are confirmed in that both types of samples give high-contrast THz images with similar signal shape (signal enhancement for both types of surface features). The slight differences are attributed to the fact that the two samples are not of exact complementary shape. The size of the bright spot in Fig. 4.16 (a) from the protrusion is larger and remains detectable at low frequency because the protrusion itself is larger than the dent. It is important to note, however, that the image contrast in case of the dent is considerably stronger (see axis scaling in Fig. 4.16 (b)), despite the fact that it has a smaller depth range than the protrusion, because the signal strength at each pixel is determined by the curvature of the respective surface element of the sample, and not by the height difference with respect to other elements. Also, the expected strong enhancement of the relative intensity at higher frequencies is observed.

In spite of the impressive sensitivity to detect surface features of small height (depth), this dark-field imaging technique does not allow the distinction between protrusions and dents. This issue motivated a second measurement technique, presented below, which does not have such a high sensitivity but introduces the ability to distinguish between convex- and concave- shaped objects.

4.5. Approach 2   - Out-of-focus detection -
4.5.1. Principle

The measurement principle is sketched in Fig. 4.17 (a). Compared to the former approach, the spatial filter is left out. The key feature of this approach is that the detection occurs out of the focus of the second lens (the focus being marked as position (2)), at a certain distance (in this case, 5 mm) in front of the focus (detector position (1)) or behind it (detector position (3)).

Fig. 4.17 (b) and (c) illustrate the effect of the out-of-focus detection with results of Helmholtz model calculations. The parameters of the model (if applicable) are as mentioned before. The graphs of Fig. 4.17 (b) display the spatial profile of the signal amplitude at the detector position, i.e., before the detection process, for the cases that the THz beam reflects off a flat surface (blue lines), the center of a dent (green lines) and the center of a protrusion (red lines). The focus is shifted away from the last lens, if the THz beam reflects off a concave surface (such as the center of the dent), and it is shifted towards the lens if the surface is convex (such as the center of the protrusion). At the detector positions marked as (1) and (3), these differences lead to marked and specific modifications of the beam profiles. Interestingly, within the validity of reducing the

sample topography into a phase mask, a detector positioned at center position (2) is insensitive to these variations.

The imaging conditions are such that the same total THz power reaches the detector planes for all three types of surface structure. In order to take advantage of the differences of the signal profiles for the distinction of convex and concave shapes, one again performs spatial filtering of the THz beam. To do so between the lenses is ineffective as I have tested numerically. I choose to perform blocking at the detector plane, in fact even without placing a beam stop or an aperture into the beam path but by taking advantage of the natural filtering which o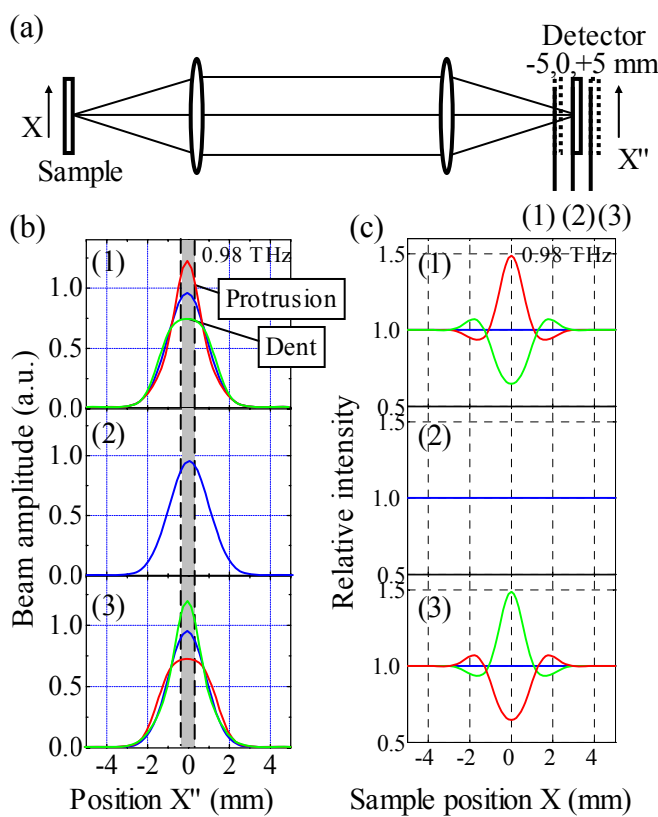ccurs when a THz signal is detected electro-optically with the help of an optical probe beam of limited diameter. The electro-optically interrogated detection region is indicated in Fig. 4.17 (b) by the shaded area having a diameter of 0.5 mm (as in the calculations of the data of Fig. 4.14).

Fig. 4.17 (c) displays the calculated detected intensity as a function of the sample position. Other possible filtering effects such as acceptance-angle restrictions are not considered.

The data of Fig. 4.17 (c) show that a detector at position (2) is insensitive to the surface topography, while placing it at position (1) or (3) introduces a pronounced dependence of the detected THz intensity on the shape of the sample surface. A closer look at the upper panel of Fig. 4.17 (c) reveals that a detector at position (1) (i.e., shifted towards the lens) sees an enhanced signal if the radiation

Figure 4.17. (a) Scheme of out-of-focus detection. The coordinate *x"* denotes the line profile direction in the three detector planes. (b) Calculated line profiles of the amplitude of a 0.98-THz beam at the three detector planes marked as (1) to (3). The blue lines represent a THz beam coming from a flat surface, the green lines mark a dent, and the red lines a protrusion. (c) Calculated detected THz intensity at the three detector positions (1) to (3) and for the three types of surface features (blue, green, red lines).

comes from a convex-shaped surface segment. This is the case in the center of the red curve representing the signal of the protrusion which is convex-shaped in the middle and concave at the periphery; and it is the case in the wings of the dashed curve calculated for the dent which is convex at its periphery. The results of calculations at different THz frequencies (not shown) reveal similar trends as those of the dark-field technique in terms of increasing signal contrast with increasing frequency.

4.5.2. Experimental result

Fig. 4.18 displays corresponding experimental results for the sample with the dent (a) and the one containing the protrusion (b). The experimental parameters are as stated above. The left column shows data taken with the detector at position (1), i.e., shifted towards the lens, as a function of the sample position. As predicted by the calculations, the dent leads to a reduced signal in the center of the measured profile, while the protrusion enhances the signal there. At detector position (3) (data shown in the right column) the signals are inverted. Hardly any effect is observed at the central detector position (2) (middle column). The measured data hence corroborate the main predictions of the Helmholtz theory.

Other observations also are fully consistent with theory: (i) the ring-like signals around the bright (dark) center features of the THz images result from the change of curvature at the periphery of the

(a) Sample with dent

Detector position:

-5 mm   0 mm   +5 mm
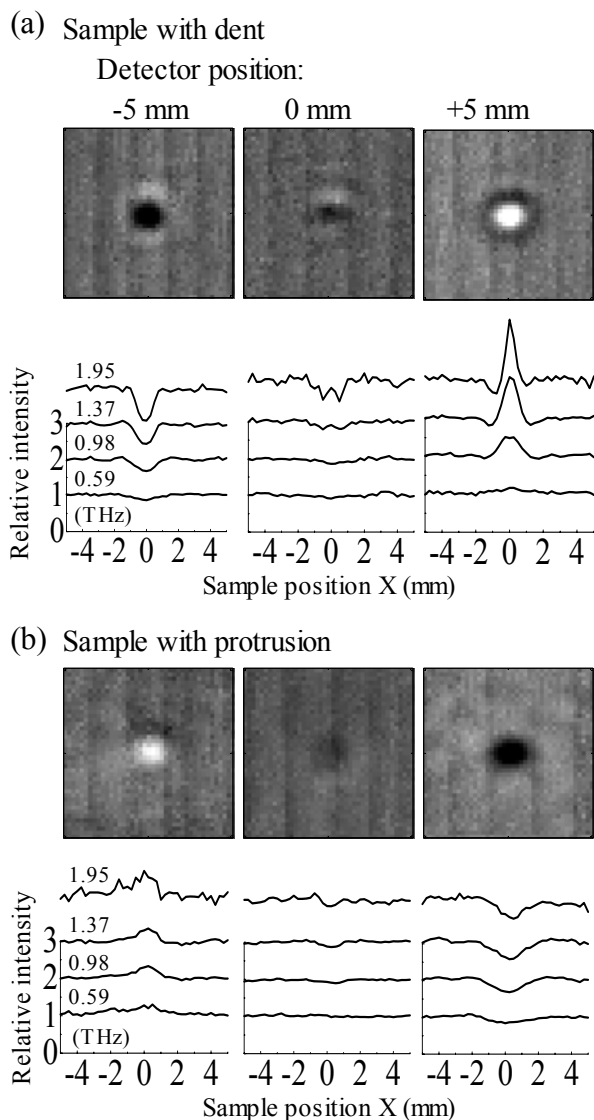

(b) Sample with protrusion

Figure 4.18. Out-of-focus detection of THz pulses. Displayed are experimentally measured intensity profiles for the 0.98-THz Fourier component, and line-scan data extracted from such profiles for four different Fourier components. Left to right column: Variation of the detector position in accordance with the notation of Fig. 17. (a) Sample with dent, (b) sample with protrusion.

surface structures, as discussed above. (ii) Similar to Fig. 4.16, the protrusion provides lower contrast than the dent because the surface curvature is weaker. (iii) The signal weakens if the frequency is reduced, an effect which mainly arises from the increase of the focal spot size at the sample position for lower THz frequencies.
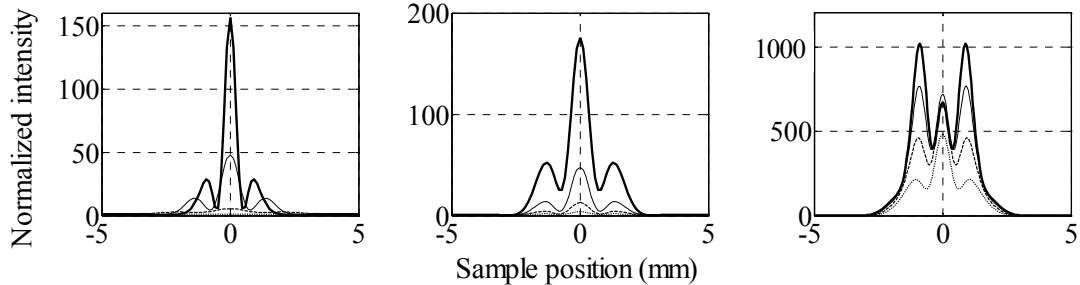
4.6. Possibility of classification and its limit

It is often important for our inspection to classify the objects, based on the 3-dimensional information, even including the object height (depth) and gradient as well as the superficial shape. As you saw previously, the dark-field detection out of two

(a) Out-of-focus detection
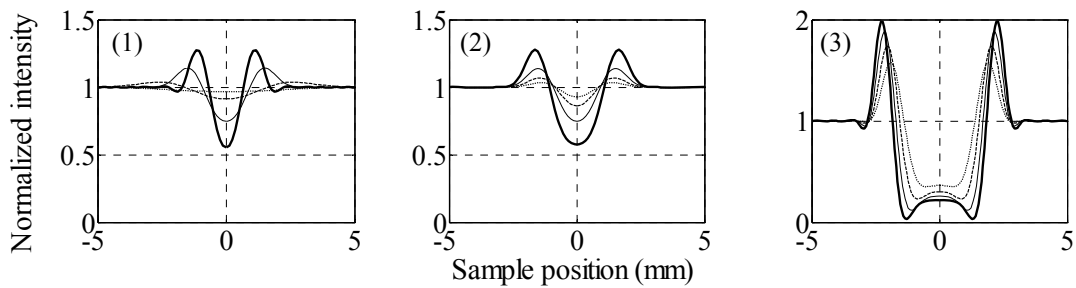
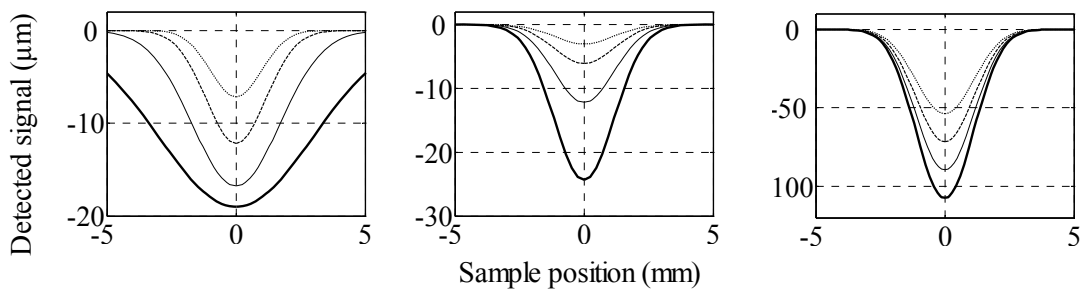(b) Dark-field detection

(c) Phase detection

Figure 4.19. Calculated signal patterns by (a) out-of-focus; (b) dark-field; (c) phase detection method. Each graph (1) indicates variation of 1 (thick full line), 2 (thin full line), 4 (dashed line) and 8 mm (dotted line) in object width, (2) 5 (dotted line), 10 (dashed line), 20 (thin full line) and 40 μm (thick full line) and (3) 75 (dotted line), 100 (dashed line), 125 (thin full line) and 150 μm (thick full line) in depth.

methods which I proposed can detect them with high sensitivity, while it is impossible to distinguish between the convex and the concave shape. The other method, the out-of-focus detection, has no problem with such distinctions. In fact, the points of classification are the following; classification i) by the outward shape (simply represented by width), ii) by the height or the depth including a discrimination between convex and concave shape, and iii) by the cross-sectional profile. In this section, I consider a possibility of these classifications, only with calculations, mainly viewed in an angle of cross-section profile, because it is comparatively harder to get information which is reflected by the cross-sectional profile than to get the 2D shape in the remote-sensing field. I also mention some comparison between the proposing methods and the phase detection like the time-of flight.

First of all, examples of signals with dents are shown in Fig. 4.19. Each line represents the calculated result by (a) the out-of-focus, (b) the dark-field and (c) the phase detection method and each column with several (1) widths of 1, 2, 4 and 8 mm (20-μm depth), (2) depths of 5, 10,20, 40 μm and (3) 75, 100, 125 and 150 μm (2-mm width). Please take note here that the THz beam and the object profile were handled as a 1-dimensional data, in order to describe a steeper slope, with avoiding an aliasing problem in the Fourier transform. All the results are cited as representative dependences on such structures, under the same condition of 1.84 mm diameter at 0.98 THz as in the section 4.5.1. Fig. 4.19 implies that all the three methods surely yield signal changes depending on the width and the depth of objects. The position of the side peaks by the out-of-focus detection, shown in (a)-(1), shifts outward and the absolute intensity weaken as the object width increases. The signal intensity increases by more than 10 times during the depth change of 5 to 150 μm, in (a)-(2) and (3), though the wings are not located in a fixed position. Next, the signals by the dark-field detection (b) which consists of three positive peaks have nearly the same tendency to such a change of the width and the depth as by the out-of-focus detection, except for two the points that the wing position is stable (see (b)-(2)) and that it has relatively high sensitivity. Both of them, (a) and (b)-(3), also have an impressive signature that the signal pattern itself is deformed, accompanying a rebound around the center area with the depth of over 100 μm. On the other hand, the phase detection gives different characters in the signal pattern. With a wider object size ((c)-(1)), the width of the signal increases, but the absolute intensity shows also a higher value. The peak value is less than the actual depth in such a case as the object width is not much bigger than the THz spot size, although this method in itself can measure the actual depth (height), besides distinguish between the convex and the concave shapes. The change of the intensity

rather than width is predominant with the object widths of less than 4 mm. It has the same dependence on object depth, as others, that the intensity increases without any pattern changes as the shape goes deeper, in spite of the absolute value less than the actual depth.

Next, I will move onto the subject of dependence on the cross-sectional profile. Fig. 4.20 (a) indicates a series of object structures which includes several gradients, while in common have a

Figure 4.20. Variation of object structure described by Super-Gaussian function with a power of 1 (dotted line), 2 (dashed line), 5 (thin full line) and 40 (thick full line). Calculated signal to the 4 types of object structures by (b) phase detection, (c) out-of-focus and (d) dark-field detection.

2-mm-width and a 20-μm- depth. The gradient is described by a power of the Super-Gaussian function, 1, 2, 5 and 40, from a dent- to a groove-like shapes. A

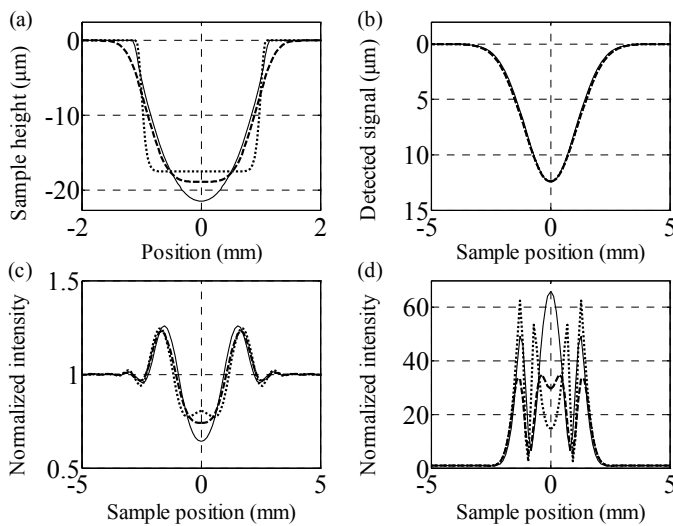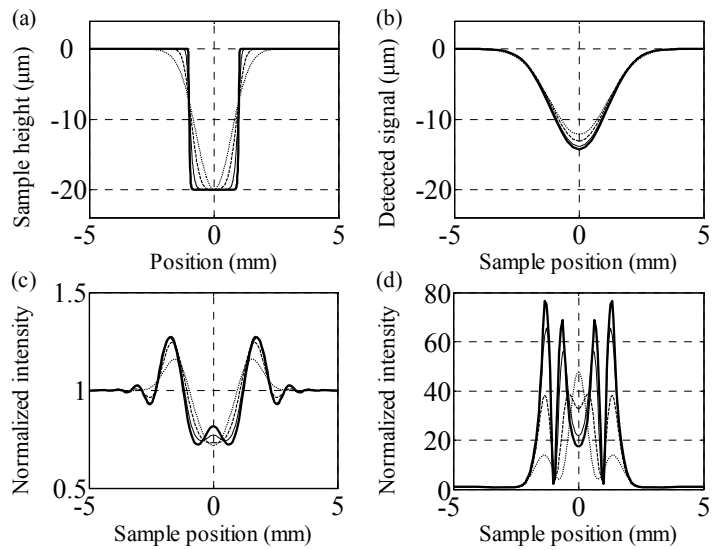Figure 4.21. Variation of object structure described by Super-Gaussian function with a power of 20 with a peak value of 17.5 μm (dotted line), 2 with 19-μm-depth (dashed line) and by a part of 25 mm diameter sphere with a peak value of 20.4-μm-depth. Calculated signal to the 3 types of object structures by (b) phase detection, (c) out-of-focus and (d) dark-field detection.

calculated signal pattern (Fig. 4.20 (b)) by phase detection indicates that the intensity is capable of slightly changing, related to the sectional structure, because a ratio of the planar parts dominates the maximum intensity. The peak value is not also consistent with the actual depth, 20 μm, from the above-mentioned reason. It is here important to note that these types of structures lead to a similar signal change with only one peak to one by depth or height variations. This implies that it

may have a limit to discriminate such structures. Meanwhile, the signals by the out-of-focus detection (c) produce a clear signature, accordant with the sectional structure. The signal gradient forming the center dip goes up and at the same time, two positive wings become stronger as the structure includes steeper edge. In case of the dark-field detection (d), a striking change from a signal pattern with a center peak and two side lobes, if the object is dent-like, to one with four sharp peaks if groove-like, is also shown. These changes reflect a shift of from the reflectional to the diffractional behavior of the THz beam, caused from the sharp edges.

Finally, I cite an instance that the phase detection is not adequate to classify the non-planar structure. Fig. 4.21 (a) shows three types of the concave structures, a rectangle groove with 17.5 μ m depth (dotted line), a trapezoidal groove with 19 μ m depth (dashed line) and a void by a 25-mm-diameter sphere (solid line) shapes, respectively. As you can see, each shape has a different curvature or a gradient. The distinction among them is often required in our inspections. However, the signal patterns by the phase detection (b) don't give a clear signal difference among them. On the other hand, the out-of-focus detection (c) yields a small signature that the pattern in the center dip is changeable to the actual structure, though the wing pattern has a slight difference. The dark-field detection (d) brings similar tendency at the center peak to one by the out-of-focus, but with more signal change, besides even the intensity of the outer peak is changed, consistent with the gradient of the objects. These results indicate that the latter two methods are capable of such a classification in principle, though a detailed examination should be needed at a step of the practical uses.

4.7. Stability of the detection system

For the purpose of introducing the THz technique to the productive manufacture, it is important to have known such system stability as dependence on a sample offset with a flat surface, for there is often a possibility that the objects may be fluctuated in a step of practical use. While examples here are obtained only by calculations, I estimated the stability against the sample offset.

Fig. 4.22 (b) indicates the detected signal amplitude as a function of the detector position (Zd in Fig. 4.22 (a)), under an assumption of the flat sample surface. Each line means a result with inserting a different beam-stop size of 5 to 20 mm diameter. In this case, the change of the signal amplitude is quite symmetry, because the Gaussian beam follows a propagation rule with a symmetrical beam radius change to a focal plane. A small signal reduction within 2 % per 2 mm is observed, independent of the beam-stop size.

In contrast, the detection signal gives a clear asymmetrical dependence on the sample position (Zs in Fig. 4.23 (a)), shown in (b). The peak position is also shifted backward when
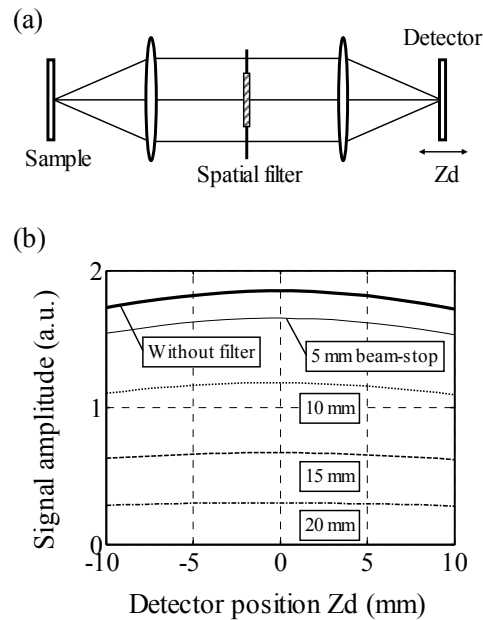

Figure 4.22. (a) Scheme of detection system. (b) Calculated detected signal as a function of the detector position without and with various sizes of beam stop, located at the spatial filter position in (a).

the size of the beam-stop increases. These are caused by the propagation in the 2-f configuration, accompanying initial misalignment (at the sample position). The beam size and the curvature at the spatial filter location (position (1) in Fig. 4.23 (a)) show completely different values in each situation. The tendency is induced from a combination of two effects, that the sample shift to the negative/positive direction makes the beam size larger/smaller at the position (1), and according to this, the larger/smaller beams at the position (2) are more tightly/loosely focused on the detector. This result also is consistent with the calculation in section 2.3.1., though I don't go into more detailed discussion. The signal change is almost 8% per ±1 mm sample shift. It is however worth noting that there is a possibility for the detector position to compensate for this asymmetry.

Fig. 4.23 (c) gives an example of signal amplitude with a flat sample surface, as a function of the sample position. Please take notice that each line represents some cases in the various detector positions, at distances (Zd') of 110 to 130 mm from the 2nd lens. At the optimized detector position, 115 ± 2 mm, the background instability against the sample offset is controlled down to 1.2 % per ±1 mm.

4.8. Future vision

I introduce an optimization of the THz reflectometry aiming at a sensitive detection for the curvature of the surface structures. The means by which this is achieved – the beam filtering and the out-of-focus detection – allow the detection and the distinction of the convex and the concave shapes. Very high sensitivity is obtained with the dark-field imaging which can enhance the signal intensities by more than 250 times (at 1.95 THz in case of the dent of 2-mm width and 20-μm height). The data evaluation suggests that one should be able to obtain useful signals from a curved surface even if it has just a few-ten micrometer of depth (height). These two THz techniques have the advantage that they simultaneously measure in the multiple frequencies and thus provide sets of the signal patterns which opens the possibility to analyze the surface topography in detail, and to classify the surface structures. However, in order to realize a reliable inspection, it is also required to utilize the information from both methods. Finally, I propose a couple of ways which can combine them (Fig. 24).
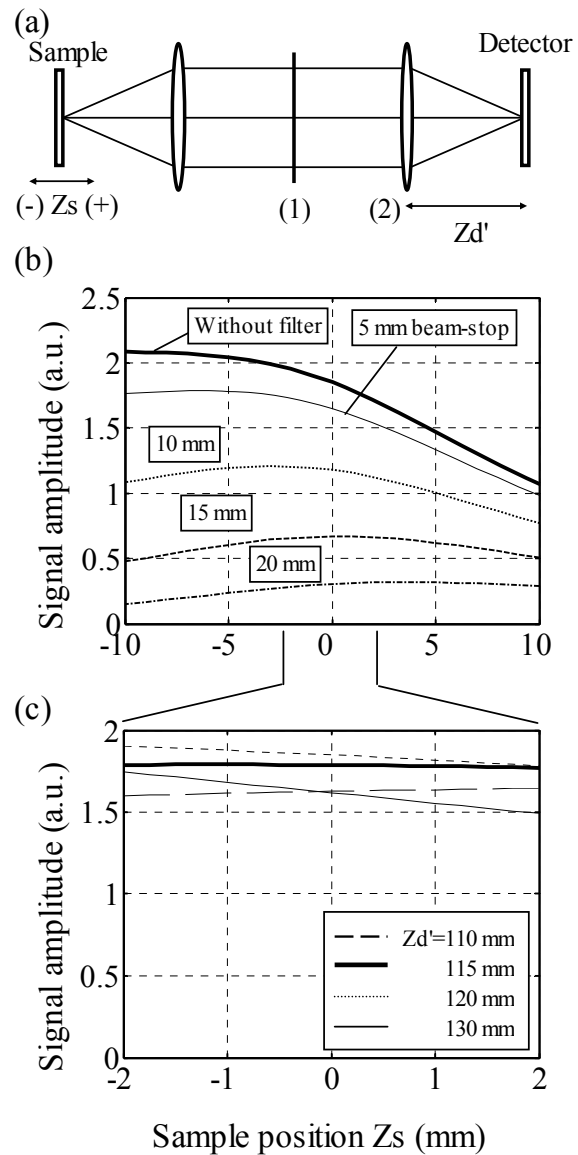

Figure 4.23. (a) Scheme of sample offset. Zs means the amount of the offset and +/- sign its direction. (b) Calculated signal amplitude as a function of sample offset with various beam stop sizes at position (1) in (a). (c) Calculated signal amplitude as a function of sample offset with various detector positions.
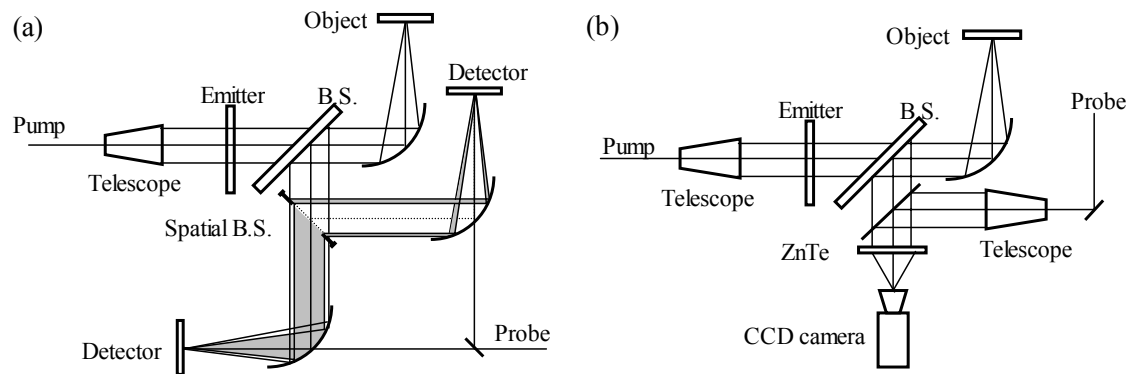
Figure 4.24. Proposed setups for a reliable inspection. (a) Multi-detection system by out-of-focus and dark-field techniques. (b) CCD camera system with adaptive filtering technique by using image processing.

The first system is established by inserting a spatial beam splitter, which acts as a circle shape to the THz beam in an angle of 45 degrees and reflects only larger than 20-mm-diameter area. The reflected beam is detected in the same way as the dark-field detection, while the rest of the beam is transmitted the beam splitter and then guided an off-focused detector. The second possibility is needed to employ a CCD camera in the detector. This system can detect the whole reflected THz beam pattern by expanding the probe beam with large-sized ZnTe crystal. An example of the opto-electronic detection with the CCD camera is already reported, but it shows a possibility to bring a decline of signal-to-noise ratio. So I should design and estimate it carefully as introducing, while it has such attractive features as a robustness to the surface conditions (like a sample offset and an angle change), by following the center position of the reflected beam and as a multi-detection which can simultaneously create several different sizes of the spatial filtering, with the image processing technique.

I hope that these THz techniques have possibilities to break a new ground in the field of the steel surface inspection.

5. High-temperature measurements

5.1. Motivation

High temperature processes in steel manufacture are important to dominate properties of final products, such as ductility and malleability. It is, there, required to control a slight amount of impurities and a condition of various dielectric materials, such as SiO_2 and CaO, which contacts with iron or steel at a temperature of 1000 to 1700 degrees. However, it has been very difficult to monitor their conditions even if the objects are electrical insulators. If it were possible to measure a thickness, molten/non-molten condition or ingredient of the dielectric materials on-line, they would realize to minimize an input energy and to make some products with higher quality.

As mentioned in the 1st chapter, the THz technique has also some advantages for a high temperature measurement, such as to naturally decrease an influence of a thermal radiation compared with the visible and the infrared light, to detect a transmitted wave from a material which has a relatively high electric conductivity because of the high S/N ratio and to be able to know its frequency dependence with a short pulse measurement. The objective of this work is to grasp the potential of the THz technique for the high temperature measurements of the complex refractive index, the electric conductivity and the simple thickness and so on, through exploring a THz behavior to some materials.

In principle, a THz measurement at a high temperature of more than 1500 degrees is needed for the purpose, but I performed a basic verification up to around 1000 degrees by using substitutive materials which have lower melting points than the SiO_2/CaO system, because it was quite hard to make up an oven which can reach 1500 degrees under the condition that the THz beam could pass it through.

5.2. Theory

5.2.1. Electric conductivity

When a crystal has a band gap energy of E_g and a simple parabolic band edge, the carrier density in the conducting band is generally described by

$$np = 4\left(\frac{k_B T}{2\pi\hbar^2}\right)\left(m_e m_h\right)^{3/2}\exp\left(-E_g / k_B T\right), \tag{5-1}$$

where n, p, m_e and m_h represent the density of and the effective mass of the electrons and holes, and k_B means the Boltzmann's constant, respectively [79]. The equation is located in an expression of the law of mass action, and $n = p$ is satisfied for

intrinsic materials. This clearly indicates that the carrier density is dependent on the term $E_g / k_B T$ in the region of the intrinsic temperature region. On the other hand, the electric conductivity is expressed as a summation of the contribution of the electrons and holes,

$$\sigma = ne\mu_e + pe\mu_h,$$ (5-2)

where μ_e and μ_h mean the mobility of the electrons and the holes. For the ionic crystals, the holes aren't essentially moved and just hop among ions by a thermal hopping process. It is known that the mobility depends on the power of the temperature (not so large), thus the temperature dependence of σ is determined by the sum of the carrier densities.

5.2.2. Multi-phonon absorption

It is thought that the absorption of the far-infrared light in alkali halides is caused from higher-order lattice potential energy by an ionic displacement, e.g. third order for 2-phonon and fourth for 3-phonon processes [80]. The phenomena are described by a phonon sum process that creates some phonons in a wavelength region of shorter than the fundamental resonance, and by a phonon difference process with destruction and creation of phonons in the longer wavelength [81, 82, 83]. Some models have been proposed for each mechanism, but here, I take up a model of the two- and three-phonon difference processes for an analysis of the data in the THz region.

i) Two phonon process

An important contribution to the absorption is expected to arise from "vertical transitions" between 2-phonon states. Fig. 5.1 indicates a simplified dispersion diagram consist of one acoustic and one optical branch only. Here one phonon in the lower branch is destroyed while another one with the same momentum, but at higher energy, is created. The difference in the energy $\hbar\omega$ is supplied by the absorbed infrared quantum. With a quantum theoretical treatment of the transition, the absorption coefficient α is described by:
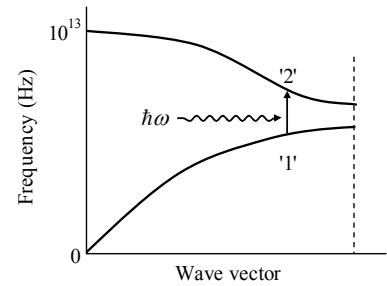

Figure 5.1. Schematic illustration of a 2-phonon difference absorption in a simplified dispersion curve [81].

$$\alpha = \frac{\pi}{2}\left(\varepsilon_0 - \varepsilon_\infty\right)\frac{\hbar\omega B^2}{\sqrt{\varepsilon_0}c\omega_0^2}\sum_{1,2}\frac{\left(n_1 - n_2\right)}{\omega_1\omega_2}\delta\left(\omega_2 - \omega_1 - \omega\right),$$ (5-3)

where B is a constant, depending on the wave vector and the branch of the phonons involved, ε_0 and ε_∞ are the low- and high- frequency dielectric constants, respectively, under an assumption that the photon frequency ω is much lower than the lattice dispersion frequency ω_0. According to Eq. (5-3), the temperature dependence of the absorption is only determined by the difference in occupation numbers $n_1 - n_2$ between the states of the energy $\hbar\omega_1$ and $\hbar\omega_2$. The occupation number in each state is

$$n_i = \left(e^x - 1\right)^{-1}, \quad x = \hbar\omega_i / kT . \tag{5-4}$$

At low frequencies when $\omega = \omega_2 - \omega_1 << \omega_1$, they state

$$\alpha \propto n_1 - n_2 = \left(\frac{\partial n_i}{\partial \omega_i}\right)\omega = \frac{xe^x}{\left(e^x - 1\right)^2}\frac{\omega}{\omega_1} = f(x)\frac{\omega}{\omega_1}, \tag{5-5}$$

where $f(x)$ represents the temperature dependent term of the absorption and is proportional to T at the high temperature.

ii) Three phonon process

When the terms of the fourth order of the displacements in the lattice are included, potential-energy processes become possible in which the photon can exchange energy with three phonons, such as $\omega_3 - \omega_2 - \omega_1 = \omega$

Figure 5.2. Variation of diagrams of 3-phonon difference absorption [81].

and $\omega_6 + \omega = \omega_4 + \omega_5$ shown in Fig. 5.2. The absorption coefficient is

$$\alpha \cong \sum \frac{\omega}{\omega_1\omega_2\omega_3}\left[n_1 n_2 - n_1 n_3 - n_2 n_3 - n_3\right] + \sum \frac{\omega}{\omega_4\omega_5\omega_6}\left[n_5 n_6 + n_4 n_6 - n_4 n_5 + n_6\right] \tag{5-6}$$

At high temperatures when $n_i = kT / \hbar\omega_i > 1$ the absorption from the term $\left[n_1 n_2 - n_1 n_3 - n_2 n_3\right]$ becomes

$$\alpha \cong \left[\frac{kT}{\hbar}\right]^2 \sum \frac{\omega^2}{\left(\omega_1\omega_2\omega_3\right)^2} . \tag{5-7}$$

The term $\left[n_5 n_6 + n_4 n_6 - n_4 n_5\right]$ similarly leads to quadratic temperature dependence.

The terms n_6 and $-n_3$, which would lead to a contribution linear in T, partially cancel, and in any cases become negligible at sufficiently high temperatures. But even if the cancellation is not complete, the major contribution from the 3-phonon difference processes will have quadratic temperature dependence. Thus, the total absorption

should approach at high temperatures is simply represented

$$\alpha = AT + BT^2 \,,$$ (5-8)

where A and B are constants [81].

5.3. Data processing

5.3.1. Numerical method of complex refractive index from THz transmittance

When a THz pulse is perpendicularly projected to a plate-like material, the transmitted amplitude is represented as summation of the multiple reflections using the transmittance $\tilde{t}_{as}(\omega)$, $\tilde{t}_{sa}(\omega)$ and the reflectance $\tilde{r}_{sa}(\omega)$ at the border between the air and the sample. If the total transmitted electric fields with and without the sample are denoted as $\tilde{E}_{ref}(\omega)$ and $\tilde{E}_{sam}(\omega)$, respectively, the ratio of their Fourier transforms can be given as

$$\frac{\tilde{E}_{sam}(\omega)}{\tilde{E}_{ref}(\omega)} = \tilde{t}_{as}(\omega) t_{sa}(\omega) \exp\left(i\frac{(\tilde{n}(\omega)-1)\omega}{c} \right) \sum_{l=0}^{m} \left((\tilde{r}_{sa}(\omega))^2 \exp\left(i\frac{2\tilde{n}(\omega)\omega}{c} \right) \right)^l$$

$$\equiv \sqrt{T(\omega)} \exp(i\phi(\omega))$$ (5-9)

where $\tilde{n}(\omega) = n(\omega) - ik(\omega)$ is the complex refractive index of the sample. Since the field $E_{ref}(\omega)$ is a real quantity, the Fourier transform will be a complex Hermitian spectrum $\tilde{E}(\omega) = E_{real}(\omega) - iE_{imag}(\omega)$ with an angular frequency ω. The exponential factor represents a phase shift and the last term the multiple reflections in this equation. The transmittance is experimentally observed a power transmittance $T(\omega)$ and a relative phase $\phi(\omega)$, however, it is difficult to analytically obtain the complex refractive index from Eq. (5-9). Therefore, a numerical method is often applied after the following transformation [84];

$$n(\omega) = \frac{c}{d\omega}\left(\phi(\omega) + \frac{d\omega}{c} + \arg\left(\tilde{t}_{as}(\omega)\tilde{t}_{sa}(\omega) \sum_{l=0}^{m+1} \left((\tilde{r}_{sa}(\omega))^2 \exp\left(-i\frac{2\tilde{n}(\omega)d\omega}{c} \right) \right)^l \right) \right),$$ (5-10)

$$k(\omega) = -\frac{c}{2d\omega} \ln \left(\frac{T(\omega)}{\left| \tilde{t}_{as}(\omega)\tilde{t}_{sa}(\omega) \sum_{l=0}^{m+1} \left(\left(\tilde{r}_{sa}(\omega)\right)^2 \exp\left(-i\frac{2\tilde{n}(\omega)d\omega}{c}\right) \right)^l \right|^2} \right). \qquad (5\text{-}11)$$

The complex refractive index roughly estimated from the THz pulse in the time domain are generally used as an initial value for an iterative loop wherein $n(\omega)$ and $k(\omega)$ are calculated in a self-consistent manner. By performing this cyclic procedure for only a few times, it is expected that the value would lead to a convergence.

5.3.2. Drude model

Optical properties of materials with electric carriers are described by an approximation of the free electrons in the Drude model. The electrons in the solid are forced by an external field and a gradient of temperature, while scattered by impurities and phonons and so on. As a result of solving the Boltzmann transport equation under an assumption of a constant relaxation time τ, the complex dielectric constant $\tilde{\varepsilon} = \varepsilon_1 + i\varepsilon_2$ is represented through the electric conductivity as

$$\varepsilon_1 = \varepsilon_\infty - \frac{Ne^2\tau^2}{m_c\varepsilon_0(1+\omega^2\tau^2)}, \quad \varepsilon_2 = \frac{Ne^2\tau}{m_c\varepsilon_0\omega(1+\omega^2\tau^2)}. \qquad (5\text{-}12)$$

where N is the carrier density, m_c is the effective mass of the carriers [36]. From this simplified model, the DC conductivity is expressed by

$$\sigma(0) = \frac{Ne^2\tau}{m_c}, \quad \tau = \frac{\varepsilon_\infty - \varepsilon_1}{\omega\varepsilon_2}. \qquad (5\text{-}13)$$

When the refractive index $\tilde{n} = \sqrt{\tilde{\varepsilon}}$ is experimentally obtained, the conductivity is calculated by this relation.

5.4. Development of experimental setup

I adopted a 2-step approach for establishing a technique of the high temperature measurements. The first one is to realize a THz transmittance measurement with a sample in a solid state, and the second in a molten state. As you can easily imagine, the measurements of the molten sample are performed under more complicated condition than of the solid sample in a point that other materials like a crucible or a window are unavoidably measured at the same time. Thus, I inspected the technical problems using

a relatively simple oven setup, first of all.

5.4.1 Setup for a basic inspection and its technical problem

A typical THz transmission setup, except an oven and a larger scale of distance, is employed, shown in Fig. 5.3. The THz pulse is emitted from the large-aperture GaAs in the same condition as the setup in Chapter 2 and the signal is detected by the electro-optical method. The THz beam is horizontally passed through a tube-type silicon-carbide oven with a 300 mm length and a 40 mm of an internal diameter. A plate like sample is vertically stood at the center of the tube mounted by a specially designed stand. The oven can raise it up to more than 1250 degrees under a condition that the both sides are open. For making the THz beam pass through the oven, it has to propagate in a distance of almost 2 m.
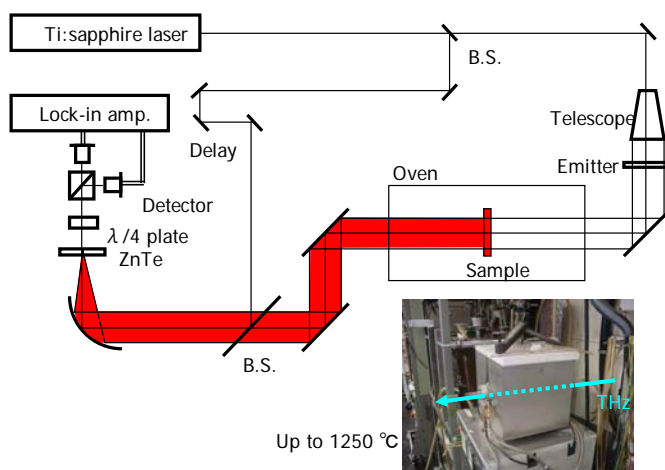

Figure 5.3. Experimental setup for a technical inspection.

Fig. 5.4 shows temperature dependence of the THz time domain data without any samples, as a reference signals, using the setup. A continuous decrease of the peak amplitude is observed when the temperature goes higher than 400 degrees. This phenomenon can't be explained by the absorption property of the air, so there is no ways except an experimental problem. I assumed that the thermal radiation from the oven tube is focused onto the EO crystal as a part of the detector. In this condition, there is a possibility that the temperature inside the crystal is locally raised and its sensitivity becomes worse.
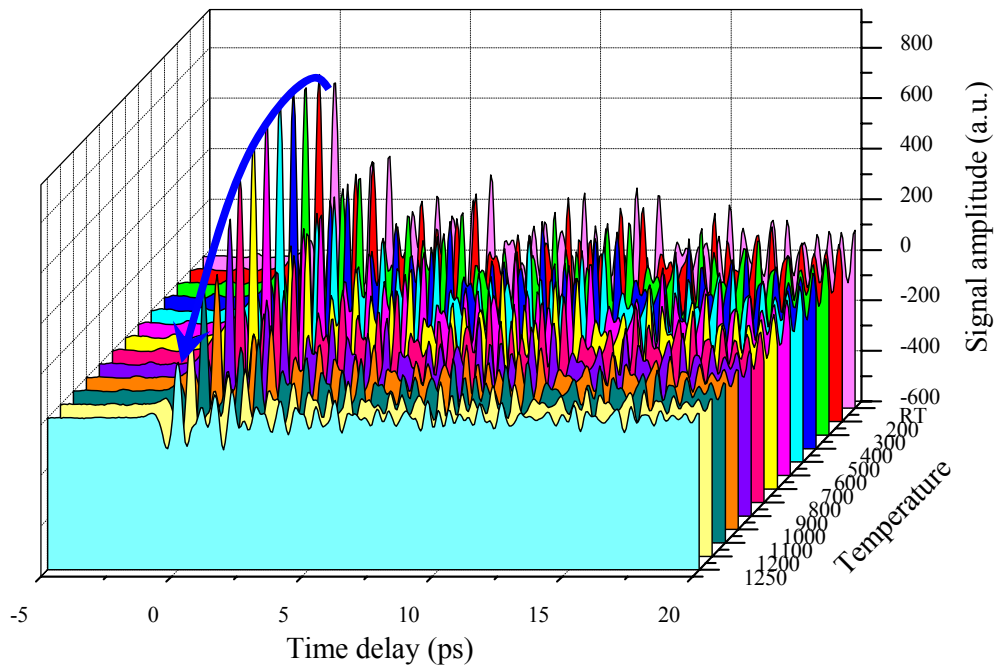
Figure 5.4. Time domain data without any samples at room temperature up to 1250 degrees. The arrow indicates the change of the peak amplitude of the main pulse.

5.4.2. A solution

If the assumption is right, a filter which is ideally transparent in the THz region and, at the same time, opaque against the infrared light should fix the problem. I directly estimated two kinds of materials, a polyethylene (PE) and a suprasil (synthetic quartz glass for fiber optics), often used as a THz window. Fig. 5.5 indicates the peak amplitude of the detected THz signal at room temperature, 400 and 1200 degrees, in cases of that a PE plate with 5 mm thickness, a suprasil plate with 2 mm and no filters are inserted into the position between the oven and the beam combiner in Fig. 5.3. The signal amplitude clearly goes
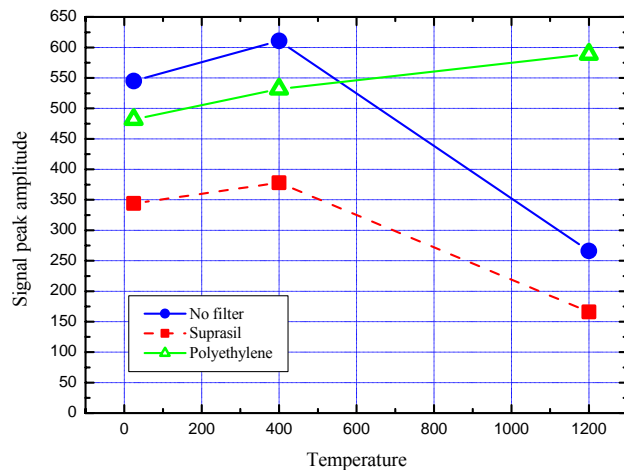

Figure 5.5. Signal peak amplitude as a function of temperature. The measurements are executed without any filters, with a 2-mm-thick suprasil and with a 5-mm-thick polyethylene plate.

down at 1200 degrees without any filters, corresponding to the time domain data in Fig. 5.4. With the suprasil filter, the tendency doesn't change, except for the low transmittance. On the other hand, there is no indication of the signal decrease with the PE plate, far from it, the data gives a slight increase as the temperature goes up. Besides, it is found that the PE is suitable for the purpose, because the transmittance of about 90 % is remarkably high, compared with the suprasil (63 %). It is thought that the increase, following the higher temperature, comes from the removal of the vapor inside and around the oven tube, and the effect is conspicuously observed at room temperature to 200 degrees. Fig. 5.6 shows an improved time domain data as a reference. It obviously indicates that the signals have the same shape without any drops at high temperatures.
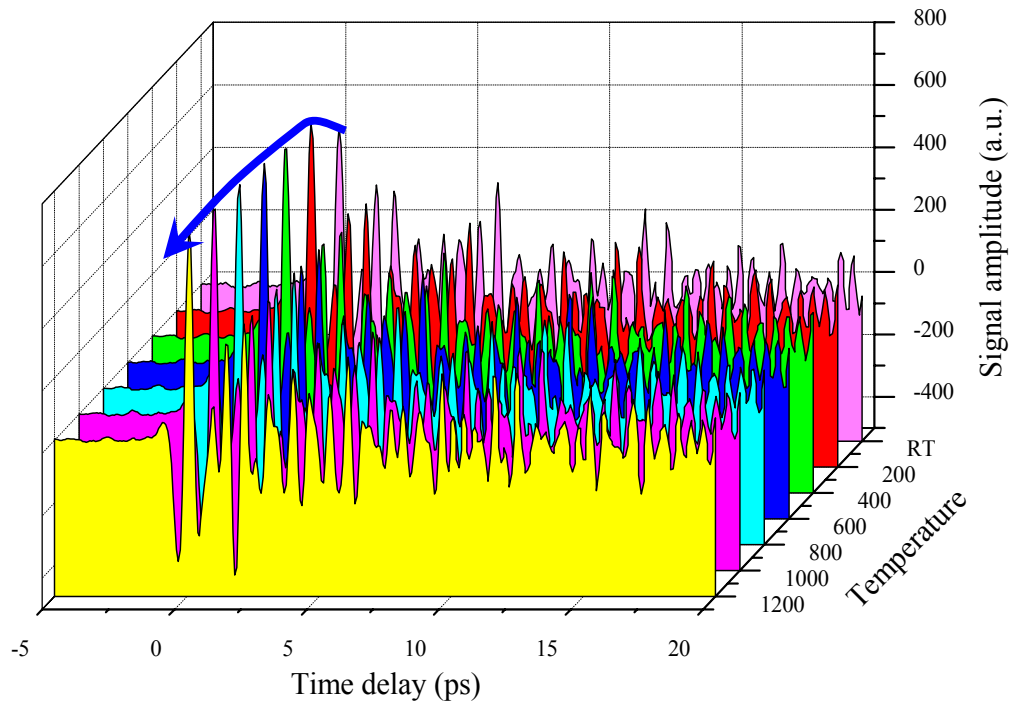

Figure 5.6. Time domain data with a polyethylene window under the same condition as Fig. 5.4.

5.4.3. Setup for molten samples

A vertical beam path is needed for the THz transmittance measurements in the liquid samples. But there are the following three problems on the practice; (i) a large hole with few cm disturbs the temperature to rise, (ii) heated air goes up (a chimney effect) and it can destroy optical components and (iii) a heat-resistant crucible which is made of a THz transparent material and which has flat surface in a precision of infrared wavelength is needed.

Against these problems, I employed the following measures;

(i) To make holes at the top and bottom sides of the tube smaller, the THz beam is loosely focused by a pair of long-focal-length lenses. Finally, I selected 180 mm PE lenses which can make the THz spot size less than 1 cm diameter at the center of the oven tube, because the thermal insulator in the oven is at least 300 mm thickness. Furthermore, there is an advantage that the lenses cut the thermal radiation, simultaneously.

(ii) A THz transparent and heat-resistant window is established on the top of the oven. I employed a 2-mm-thick suprasil plate although the transmittance is comparably low.

(iii) I manufactured a special crucible made of sapphire and a new sample holder which can switch two states with only the crucible and with a sample and the crucible. The actual setup is illustrated in Fig. 5.7.
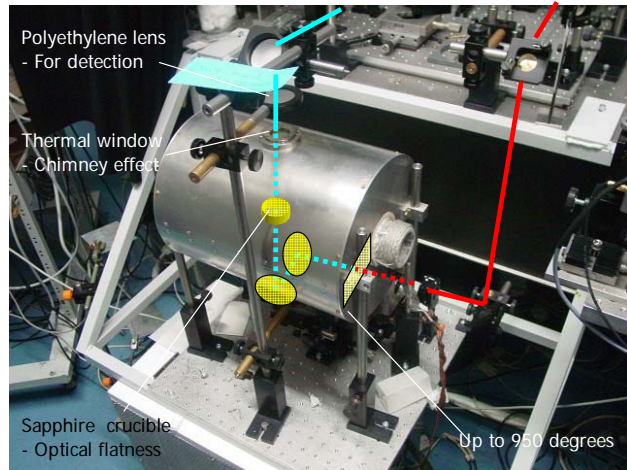

Figure 5.7. Experimental setup for molten samples.

5.5. Experimental data and discussion

Fig. 5.8 (a) shows time domain data of a 1-mm-thick KBr. These were measured in a temperature step of 100 degrees using the setup mentioned in the section 5.3. To minimize the influence of the thermal expansion of the suprasil window and the sapphire crucible, the two states of the sample holder is switched at every temperature. Each data is averaged 5 times. You can find that the peak amplitude decreases and the peak position is delayed as the temperature increases. The Fourier spectra of these data, shown in Fig. 5.8 (b), indicate that the transmittance becomes lower when the frequency and the temperature go higher. Especially, the transmittance is close to zero with a sample in a molten state.

For your reference, another data of a 2-mm-thick KCl crystal is shown in Figs. 5.8. (c) and (d). The difference is that the measurement was performed without the crucible and the suprasil window for verifying of their influence, although in a rougher step of 250 degrees. It clearly indicates that the same tendency of the waveform change in the time domain, the temperature and the frequency dependence in the Fourier space as the case of the KBr sample.
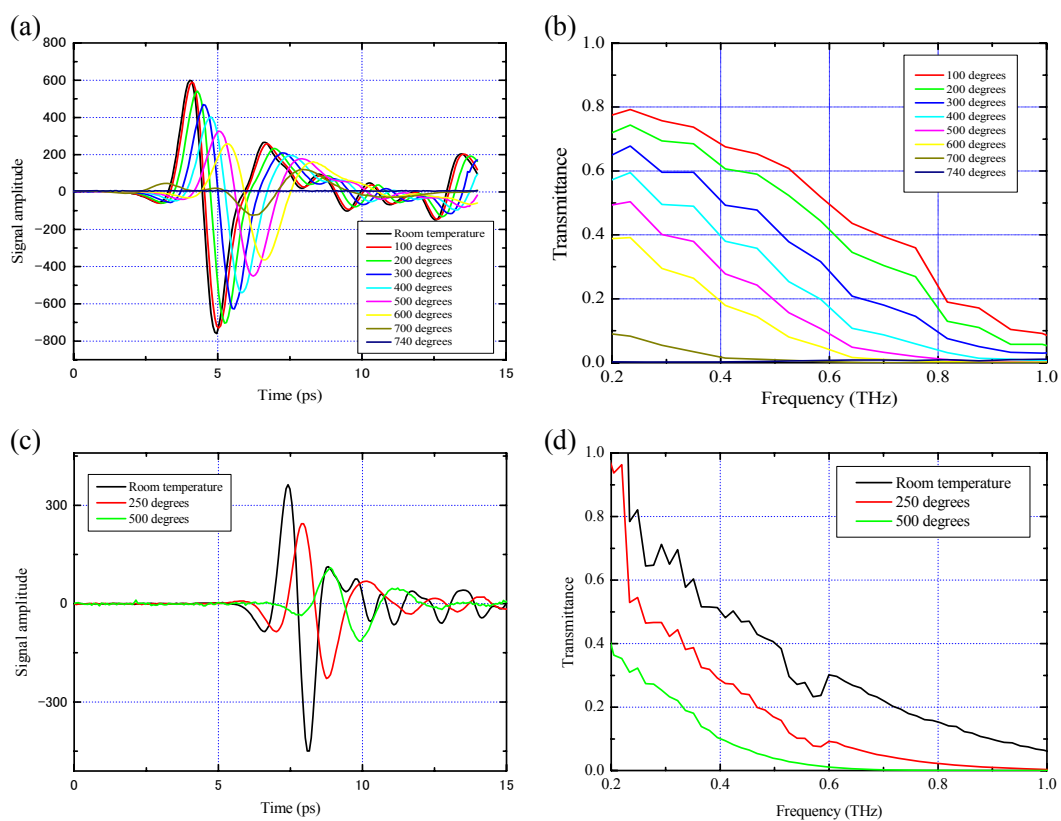
Figure 5.8. Time domain data of (a) KBr, (c) KCl, and their Fourier spectra of (b) KBr , (d) KCl, respectively.
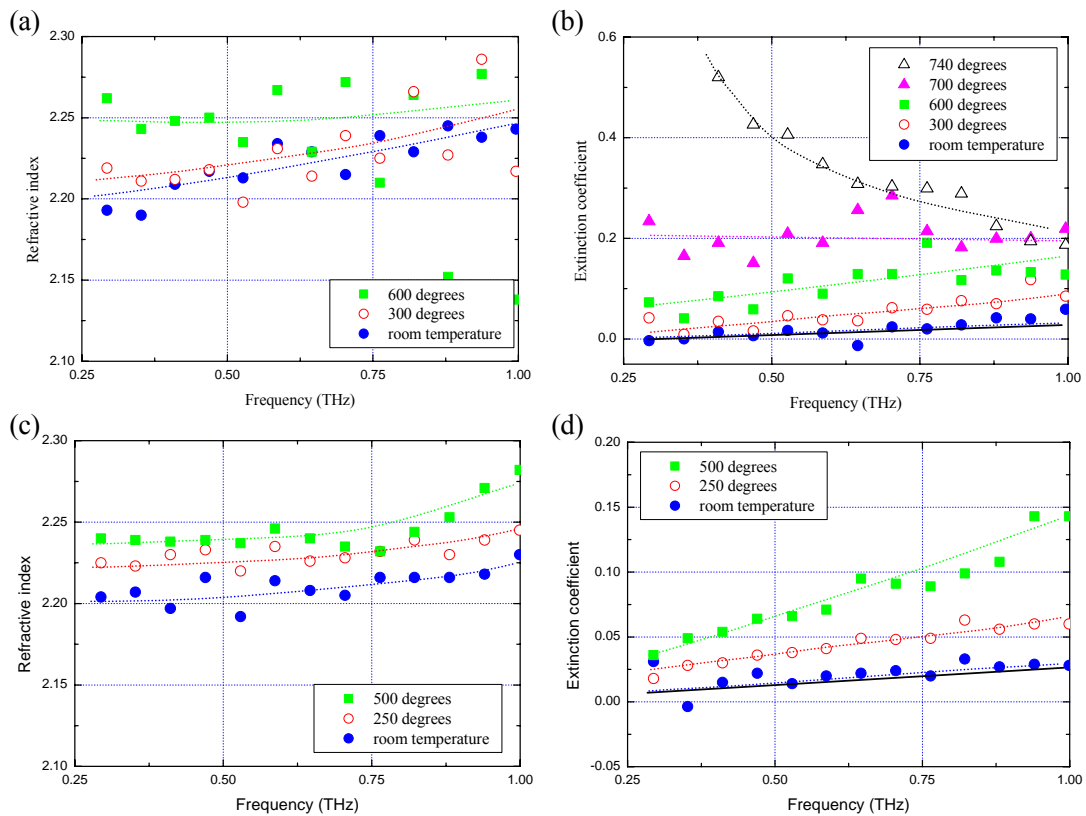

Figure 5.9. Refractive indices of (a) KBr, (c) KCl, and extinction coefficients of (b) KBr, (d) KCl, calculated from the experimental data.

- 54 -

I transformed these data into the complex refractive indices using Eqs. (5-10) and (5-11). In the calculation, the thickness variation by the thermal expansion should be taken into account. According to the references, the change reaches several 10-microns per 1 mm. I adjusted the thickness of the samples at each temperature, keeping the hopping of the phase factor minimum. The values are slightly larger for the KCl sample, while a few times larger for the KBr. For the latter case, there is a possibility that the crucible makes the situation complicated. The material of the crucible, Al_2O_3, has a 1/7 smaller thermal expansion, compared to the alkali halides [85]. It is, therefore, supposed that almost all the expansion of the KBr might be occurred only one-dimensionally, parallel to the THz propagation, in this case.

The transformed data are shown in Fig. 5.9. These are enlarged in the frequency of 0.2 to 1 THz, because the signal-to-noise ratios are quite low except this region. The marks represent the measured data at the temperature corresponding to the raw data and the solid lines the other data at room temperature in the literature [86, 87]. My experimental results are well matched to the previous ones. When the temperature increases, n and k give higher values, especially in a region of high frequency. It is possible to be qualitatively explained by the facts that the width of the reststrahl band, at a frequency of 127 cm-1 for the KBr and 159 cm-1 for the KCl, becomes broader and their peak positions shift to the longer wavelength as the temperature goes up [88, 89, 90]. The reference verifies only the LiF and MgO, however it is naturally thought that their change could be the characteristic common to all the alkali halide crystals. It is here worth noting that the frequency dependence of k for the KBr sample in the molten state gives a completely different trend which yields higher values as the frequency decreases.

It was thought that the increase of the extinction coefficient at the high temperature was caused from the change of the electric conductivity, so I firstly tried to analyze these data by the theory of the ionic conductivity. The measured data is transformed into the DC conductivity using Eqs. (5-12) and (5-13) with a value of E_g =3.3 meV [79]. The result is plotted with
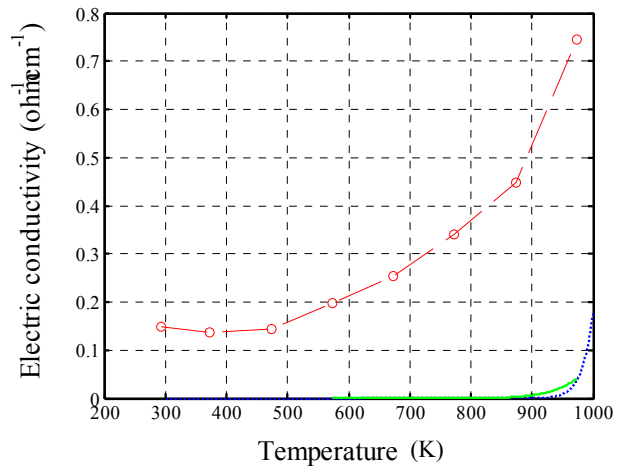

Figure 5.10. Electric conductivity of KBr as a function of temperature. The hollowed circles represent the experimental result, the solid line the formula and the dotted line the theoretical calculation.

hollowed circles in Fig. 5.10, and the results calculated by Eqs. (5-1), (5-2) and by a conventional formula with the parameter $A = 1.3 \times 10^{-4}$ and $B = 1.91$ eV;

$$\sigma = A \exp(-B/kT) \qquad (5\text{-}14)$$

are also added with a solid and a dotted line [91]. As you can see, the experimental data and the calculation results are coincident in the point of the higher k with the higher temperatures. But the experimental data apparently shows higher values even if at the room temperature. And the extent of its change doesn't indicate so large, only 10 times at 700 degrees to the room temperature for the data, while more than $10^{2\text{-}3}$ variations for the calculations. The difference among them amounts to more than $10^{3\text{-}5}$ times in a range of room temperature to 400 degrees and few times at 700 degrees. Furthermore, an estimate of the carrier density, $5*10^{-9}$ cm^{-3} (at room temperature) to $7*10^{11}$ cm^{-3} (at 700 degrees), also supports the difference. It comes to a conclusion that the crystal is a good insulator and the temperature dependence of k can't be explained by the ionic conductivity. On the other hand, it is important to mention that the value of the measurement data at 740 degrees, i.e. in the molten state, represents the same order as the other experiments [92]. These results push one to the other analysis.
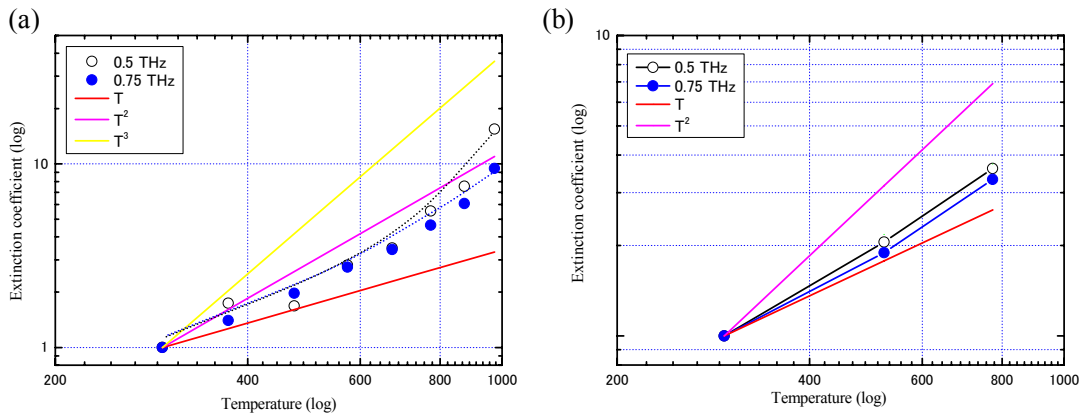

Figure 5.11 Extinction coefficients of (a) KBr, (b) KCl at 0.5 and 0.75 THz, as a function of temperature, and the solid and dotted lines represent relations T, T^2, respectively.

Fig. 5.11 indicates the extinction coefficients at 0.5 and 0.75 THz, for the KBr and KCl samples, as a function of temperature. Linear and quadratic lines from Eq. (5-8) are also plotted in the figure. The data slightly show different temperature dependence from the linear and the quadratic relations, but they are located between them. These results are considerably similar to the previous data in the reference [81, 93, 94], though the plotted frequencies of 0.5 and 0.75 THz are higher than the 0.01-0.116 THz in the

reference. The values of my data are regarded as the sufficiently lower frequency, compared to the fundamental resonance.

The data from the THz measurements qualitatively agree with the fact that the change of the extinction coefficient of the alkali halides in the solid state is dominated by the 2- and 3-phonon absorption mechanism, while k is determined by the ionic conductivity in case of the molten state.

5.6. Summary and prospect

I constructed the THz measurement technique at the high temperature, by solving the problem as to the thermal radiation. When I applied the system to measure the alkali halide crystals, the KBr and the KCl, the following terms were verified;

(1) The data of the refractive index n and the extinction coefficient k, calculated by the numerical transformation from the transmittance T and the phase shift ϕ data into n and k, are well matched to the previous data at the room temperature.

(2) The frequency dependence of the n and k qualitatively agrees with the spectral behavior by the peak shift and the broadening of the reststrahl band.

(3) The analysis of the temperature dependence of k demonstrates that the absorption mechanism up to the melting temperature is dominated by the lattice vibrations of the 3rd and 4th order displacements, while the ionic conductivity is dominant beyond the melting point.

It is observed that the THz transmittance becomes remarkably low in a molten state, caused from the increase of the electric conductivity. It is also implied that the behavior might be applied to many materials, even if it is a good insulator at the room temperature. It doesn't instantly mean that the THz technique isn't suitable to the high temperature measurements. An example of the time domain data at high temperatures is shown in Fig. 5.12. The sample is a particular material for the steel manufacturing process, containing carbon. It is known that the carbon is vanished beyond a temperature of 800 degrees, caused from a reaction of the 2C+O2->2CO. The THz data truly reflects that the chemical reaction transfers the material to the other state. Like this,
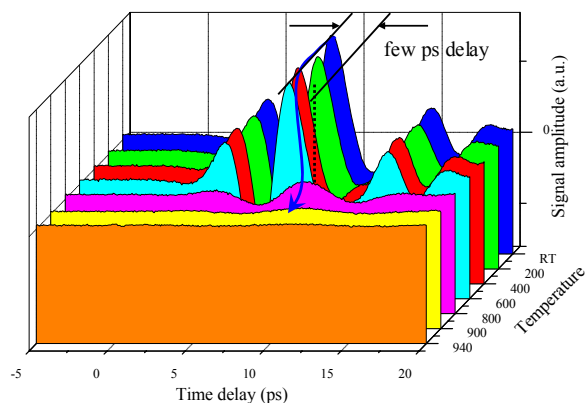

Figure 5.12 An example of time domain data of a particular material for the steel-making process.

THz technique has possibilities to open a way that the state of materials could be remotely observed, even if at high temperatures.

6. Conclusion

I demonstrated some experimental and theoretical verification on the THz measurement techniques for a purpose of applying it to the steel manufacturing processes. As you have seen above, the work is consists of three topics, (1) the spatial distribution of the THz generation from the large-aperture GaAs, (2) the THz radar for the surface inspection and (3) the high temperature technique. I briefly summarize each work.

(1) It is already known that the two screening effects, the THz radiation and the carrier dynamics, bring the saturation of the THz output power. I found the facts that the saturation level is remarkably large as the laser fluence increases and that the laser power dependence of the THz generation pattern indicates more drastic change than the former screening models predicted in case of using the high power Ti:sapphire laser. The model which is incorporated the initial carriers reproduces the THz beam profiles, the peak shift and the damping behavior of the THz pulses in the experimental data. The calculation result leads to a conclusion that the satellite pulses of the laser might be one of the chief factors. This work demonstrated that the small pulses with, at most, 10^{-3} to the amplitude of the main laser pulse bring such remarkable changes.

(2) In the radar work, I verified that the dark-field configuration gives several signal patterns corresponding to the surface profiles and that it detects them in a considerably high sensitivity down to a 10-micron order height or depth with a few-millimeter width. Furthermore, for discriminating between the convex- and the concave-shapes, I developed the out-of-focus detection. The model by the THz wave propagation gives us information their capability for the detection and tolerance against the offset of the objects.

(3) I took up the ionic crystals as good insulators, and showed some evidences that the phonon difference absorption below the melting point and the electric conductivity in its molten state are dominant to the THz transmittance. Though the molten objects bring slight transmittance as 10^{-3} order, the experimental result indicates that the method makes it possible to monitor the transformation of materials, caused from chemical reactions at high temperature.

I believe that this work can open up a possibility to realize the on-line inspection and monitoring what has never observed, so far, in the steel manufacturing processes in the future.

References

[1] D. H. Auston, K. P. Cheung and P. R. Smith, "Picosedond photoconducting Hertzian dipoles," Appl. Phys. Lett., 45, 284-286 (1984).

[2] D. H. Auston and M. C. Nuss, "Electrooptic Generation and Detection of Femtosecond Electrical Transients," IEEE J. Quantum Electronics, 24, 184-197 (1988).

[3] P. U. Jepsen, R. H. Jacobsen and S. R. Keiding, "Generation and detection of THz pulses from biased semiconductor antennas," J. Opt. Society. Am., B13, 2424 (1996).

[4] J. E. Pedersen and S. R. Keiding, C. D. Sorensen, P. E. Lindelof, W. W. Ruhle and X. Q. Zhou, "5-THz bandwidth from GaAs-on-silicon photoconductive receiver," J. Appl. Phys., 74, 7022 (1993).

[5] S. Matsuura, G. A. Blake, R. A. Wyss, J. C. Pearson, C. Kadow, A. W. Jackson and A. C. Gossard, "A Traveling-Wave THz Photomixer Based on Angle-Tuned Phase Matching," Appl. Phys. Lett., 74, 2872 (1999).

[6] X. -C. Zhang, Y. Jin, L. E. Kingsley and M. Weiner, "Influence of electric and magnetic fields on THz radiation," Appl. Phys. Lett., 62, 2477 (1993).

[7] D. You, R. R. Jones, P. H. Bucksbaum and D. R. Oykaar, "Generation of high-power sub-single-cycle 500-fs electromagnetic pulses," Opt. Lett., 18, 290 (1993).

[8] L. Xu, X. -C. Zhang and D. H. Auston, "Terahertz beam generation by femtosecond optical pulses in electro-optic materials," Appl. Phys. Lett., 61, 1784 (1991).

[9] A. Rice, Y. Jin, X. F. Ma and X. -C. Zhang, "Terahertz optical rectification from <110> zinc-blende crystals," Appl. Phys. Lett., 64, 1324 (1994).

[10] Q. Wu and X. -C. Zhang, "Ultrafast electro-optic field sensors," Appl. Phys. Lett., 68, 1604 (1996).

[11] Q. Wu and X. -C. Zhang, "Free-space electro-optics sampling of mid-infrared pulses," Appl. Phys. Lett., 71, 1285 (1997).

[12] R. Huber, A. Brodschelm, F. Tauser and A. Leitenstorfer, "Generation and field-resolved detection of femtosecond electromagnetic pulses tunable up to 41 THz," Appl. Phys. Lett., 76, 3191 (2000).

[13] E. H. Linfield, A. G. Daves, M. B. Johnston and A. Dowd, "Terahertz generation at semiconductor surfaces," Central Laser Facility Annual Report 2001/2002, 154.

[14] M. Hangyo, S. Tomozawa, Y. Murakammi, M. Tonouch, M. Tani, Z. Wang, K. Sakai and S. Nakashima, "Terahertz radiation from superconducting Yba2Cu3O7-_ thin films excited by femtosecind optical pulses," Appl. Phys. Lett., 69, 2122 (1996).

[15] C. Jackel, H. G. Roskos and H. Kurtz, "Emission of picosecond electromagnetic pulses from optically excited superconductive bridges," Phys. Rev. B, 54, R6889 (1996).

[16] M. A. Piestrup,l R. N. Fleming and R. H. Pantell, "Continuously tunable submillimeter wave source," Appl. Phys. Lett., 26, 418 (1975).

[17] K. Kawase, M. Sato, T. Taniuch and H. Ito, "Coherent tunable THz-wave generation from LiNbO3 with monolithic grating coupler," Appl. Phys. Lett., 68, 2483 (1996).

[18] K. A. McIntosh, E. R. Brown, K. B. Nichols, O. B. McMahon, W. F. DiNatale and T. M. Lyszczarz, "Terahertz photomixing with diode lasers in low-temperature-grown GaAs," Appl. Phys. Lett., 67, 3844 (1995).

[19] F. Siebe, K. Siebert, R. Leonhardt, H. G. Roskos, "A fully tunable dual-color cw Ti:Al2O3 laser," IEEE J. of Quantum Electron., JQE-35, 1731 (1999).

[20] H. G. Roskos, C. Waschke, R. Schwedler, P. Leisching, Y. Dhaibi, H. Kurz and K. Kohler, "Bloch oscillations in GaAs/AlGaAs superlattices after excitation well above the bandgap," Superlattices and Microstructures, 15, 281 (1994).

[21] R. Sachs, L. A. Banyai, E. Mohler, K. Kohler and H. G. Roskos, "Terahertz dielectric response of a moving electron gas," Proc. 26th Intern. Conf. On the Physics of Semiconductors, ICPS-26, paper P-172.

[22] R. Kohler, A. Tredicucci, F. Beltram, H. E. Beere, E. H. Linfield, A. G. Davies, D. A.

Ritchie, R. C. Iotti and F. Rossi, "Terahertz semiconductor-heterostructure laser," Nature, 417, 156 (2002).

[23] D. Strickland and G. Mourou, "Compression of amplified chirped optical pulses," Optics Comm., 56, 219 (1985).

[24] M. R. Kutteruf, C. M. Brown, L. K. Iwaki, M. B. Campbell, T. M. Korter and E. J. Heilweil, "Terahertz spectroscopy of short-chain polypeptides," Chem. Phys. Lett., 375, 337 (2003).

[25] A. G. Markelz, A. Roitberg and E. J. Heilweil, "Pulsed terahertz spectroscopy of DNA, bovine serum albumin and collagen between 0.1 and 2.0 THz," Chem. Phys. Lett., 320, 42 (2000).

[26] T. Löffler, T. Bauer and H. G. Roskos, "Terahertz dark-field imaging of biomedical tissue," Opt. Exp., 9l, 616 (2001).

[27] T. Löffler, K. Siebert, S. Czasch, T. Bauer and H. G. Roskos, "Visualization and classification in biomedical terahertz pulsed imaging," Phys. Med. Biol., 47, 3847 (2002).

[28] R. H. Jacobsen, D. M. Mittleman and M. C. Nuss, "Chemical recognition of gases and gas mixtures with terahertz waves," Opt. Lett., 21, 2011 (1996).

[29] R. A. Cheville and D. Grischkowsky, "Observation of pure absorption spectra in the v2 band of hot H2O in flames," Opt. Lett., 23, 531 (1998).

[30] R. A. Cheville and D. Grischkowsky, "Far-infrared terahertz time-domain spectroscopy of flames," Opt. Lett., 20, 1646 (1995).

[31] L. Thrane, R. H. Jcobsenl, P. U. Jespen and K. R. Keiding, "THz reflection spectroscopy of liquid water," Chem. Phys. Lett., 240, 330 (1995).

[32] B. B. Hu and M. C. Nuss, "Imaging with terahertz waves," Opt. Lett., 20, 1716 (1995).

[33] D. M. Mittleman, J. Cunningham and M. C. Nuss, "Noncontact semiconductor

wafer characterization with the terahertz Hall effect," Appl. Phys. Lett., 71, 16 (1997).

[34] R. A. Cheville and D. Grischkowsky, "Time domain terahertz impulse ranging studies," Appl. Phys. Lett., 67, 1960 (1995).

[35] D. M. MittlemanS. Hunsche, L. Boivin and C. Nuss, "T-ray tomograpphy," Opt. Lett., 22, 904 (1997).

[36] M. Exter and D. Grischkowsky, "Carrier dynamics of electrons and holes in moderately doped silicon," Phys. Rev. B, 41, 12140 (1990).

[37] T. Bauer, J. S. Kolb, T. Löffler, E. Mohler and H. G. Roskos, "Indium-Tin-Oxide-Coated glass as dichroic mirror for far-infrared electromagnetic radiation," J. of Appl. Phys., 92, 2210 (2002).

[38] M. Pessot, P. Maine and G. Mourou, "1000 times expansion/compression of optical pulses for chirped pulse amplification," Optics Comm., 62, 419 (1987).

[39] O. E. Martinez, "3000 times grating compressor with positive group velocity dispersion: Application to fiber compensation in 1.3-1.6 mm region," IEEE J. Quantum Electron., QE-23, 59 (1987.

[40] D. E. Spence, P. N. Kean and W. Sibbett, "60-fs pulse generation from a self-mode-locked Ti:sapphire laser," Opt. Lett., 16, 42 (1991).

[41] J. W. Goodman, "Introduction to Fourier Optics," McGraw-Hill, New York, second edition (1996).

[42] A. Gürtler, C. Winnewisser, H. Helm, and P. U. Jepsen, "Terahertz pulse propagation in the near field and the far field," J. Opt. Soc. Amer. A, vol. 17, pp. 74-83, 2000.

[43] M. Tani, M. Tonouchi, Z. Wang, K. Sakai, M. Hangyo, S. Tomozawa and Y. Murakami, "Enhanced sub-picosecond electromagnetic radiation from Yba2Cu3O7-thin-film how-tie antenna excited with femtosecondlaser pulses," Jpn. J. Appl. Phys., 35, L1184 (1996).

[44] H. Saijo, M Morimoto, M. Yamashita, O. Morikawa, T. Kondo, M. Tonouch and M. Hangyo, "Terahertz radiation from high-Tc superconductive log-periodic antennas," Proc. IEEE 7th Int. Conf. on Terahertz Electronisc, 245 (1999).

[45] E. E. Doany, D. Grischkowsky and C. –C. Chi, "Carrier lifetime versus ion-implantation dose in silicon on sapphier," Appl. Phys. Lett., 50, 460 (1987).

[46] G. Gupta, J. E. Whitaker and G. A. Mourou, "Ultrafast carrier dynamics in III-V semiconductors grown by molecular-beam epitaxy at very low substrate temperatures," IEEE J. Quantum Electron., 28, 2464 (1992).

[47] G. L. Witt, "LTMBE GaAs: present status, and perspectives," Material Science and Engineering, B22, 9 (1993).

[48] D. C. Look, "Molecular beam epitaxial GaAs grown at low temperature," Thin Solid Films, 231, 61 (1993).

[49] A. Yariv, "Introduction to optical electronixs," Chapter 9, New York, Holt, Rinehart and Winston Inc., 3rd edition (1985).

[50] S. L. Chuang, S. Schmitt-Rink, B. I. Greene, P. N. Saeta and A. F. J. Levi, "Optical rectification at semiconductor surfaces," Phys. Rev. Lett., 68, 102 (1992).

[51] F. Tauser and A. Leitenstorfer, "100 THz-pulses," ITW 2000 (2000).

[52] B. E. A. Saleh and M. C. Teich, "Fundamentals of Photonics," Wiley Interscience, New York (1990).

[53] C. Winnewisserl, P. U. Jepsen, M. Schall, V. Schyja and H. Helm, " Electro-optic detection of THz radiation in LiTa O3, LiNbO3, and ZnTe," Appl. Phys. Lett., 70, 3069 (1997).

[54] A. Yariv, "Introduction to optical electronixs," Chapter 2, New York, Holt, Rinehart and Winston Inc., 3rd edition (1985).

[55] J. T. Darrow, X.-C. Zhang, D. H. Auston, and J. D. Morse, "Saturation properties of large-aperture photo-conducting antennas," IEEE J. Quantum Electron., 28, 1607, (1992).

[56] J. T. Darrow, X.-C. Zhang, D. H. Auston, "Power scaling of large-aperture photoconducting antennas," Appl. Phys. Lett., 58, 25, (1991).

[57] P. K. Benicewicz, J. P. Roberts, and A. J. Taylor, "Scaling of terahertz radiation from large-aperture biased photoconductors," J. Opt. Soc. Amer. B., 11, 2533, (1994).

[58] P. K. Benicewicz, and A. J. Taylor, "Scaling of terahertz radiation from large-aperture biased InP photoconductors," Opt. Lett., 18, 1332, (1993).

[59] S.-G. Park, A. M. Weiner, M. R. Melloch, C. W. Siders, J. L. W. Siders, and A. J. Taylor, "High-power narrow-band terahertz generation using large-aperture photoconductors," IEEE J. Quantum Electron., 35, 1257 (1999).

[60]. C. W. Siders, J. L. W. Siders, A. J. Taylor, S. –G. Park, M. R. Melloch, and A. M. Weiner, "Generation and characterization of terahertz pulse trains from biased, large-aperture photoconductors," Opt. Lett., 24, 241 (1999).

[61] A. J. Taylor, G. Rodriguez, and D. Some, "Ultrafast field dynamics in large-aperture photoconductors," Opt. Lett., 22, 715 (1997).

[62] Z. Piao, M. Tani, and K. Sakai, "Carrier dynamics and terahertz radiation in photoconductive antennas," Jpn. J. Appl. Phys., 39, 96 (2000).

[63] J. E. Pedersen. V. G. Lyssenko, J. M. Hvam, P. U. Jepsen, S. R. Keiding, C. B. Sorensen, and P. E. Lindelof, "Ultrafast local field dynamics in photoconductive THz antennas," Appl. Phys. Lett., 62, 1265 (1993).

[64] F. G. Sun, G. A. Wagoner, and X. -C. Zhang, "Measurement of free-space terahertz pulses via long-lifetime photoconductors," Appl. Phys. Lett., 67, 1656 (1995).

[65] E. Budiarto, and N. –W. Pu, "Near-field propagation of terahertz pulses from a large-aperture antenna," Opt. Lett., 23, 213 (1998).

[66] D. You, and P. H. Bucksbaum, "Propagation of half-cycle far infrared pulses," Opt. Soc. Am. B, 14, 1651 (1997).

[67] E. Budiarto, J. Margolies, S. Jeong, and J. Son, "High-intensity terahertz pulses at 1-kHz repetition rate," IEEE J. Quantum Electron., 32, 1839 (1996).

[68] G. Rodriguez and A. J. Taylor, "Screening of the bias field in terahertz generation from photoconductors," Opt. Lett., 21, 1046 (1996).

[69] N. Hasegawa, M. Thomson, T. Löffler, and H. G. Roskos, "Remote identification of protrusions and dents on surfaces by terahertz reflectometry with spatial beam filtering and out-of-focus detection," Appl. Phys. Lett., 83, 3996 (2003).

[70] "Technical report 94-06," Clark-MXR, Inc. (1994).

[71] Z. G. Lu, P. Campbell, and X. –C. Zhang, App. Phys. Lett., 71, 593 (1997)

[72] T. Hattori, K. Tukamoto, and H. Nakatsuka, "Time-resolved study of intense terahertz pulses generated by a large-aperture photoconductive antenna," Jpn. J. Appl. Phys., 40, 4907 (2001).

[73] D. M. Mittleman, R. H. Jacobsen and M. C. Nuss, "T-ray imaging," IEEE J. Sel. Top. Quantum Electron., 2, 679 (1996).

[74] Q. Chen and X. -C. Zhang, "Polarization modulation in optoelectronic generation and detection of terahertz beams," Appl. Phys. Lett., 74, 3435 (1999).

[75] Q. Chen, M. Tani, Z. Jiang and X. -C. Zhang, "Electro-optic transceivers for terahertz wave applications," J. Opt. Soc. Am. B, 18, 823 (2001).

[76] J. L. Johnson, T. D. Dorney and D. M. Mittleman, "Enhanced depth resolution in terahertz imaging using phase-shift interferometry," Appl. Phys. Lett., 78, 835 (2001).

[77] J. L. Johnson, T. D. Dorney and D. M. Mittleman, "Interferometric imaging with terahertz pulses," IEEE J. Sel. Top. Quantum Electron., 7, 592 (2001).

[77] S. Nashima, O. Morikawa, T. Takata and M. Hangyo, "Measurement of optical properties of highly doped silicon by terahertz time domain reflection spectroscopy," Appl. Phys. Lett., 79, 3923 (2001).

[78] S. M. Tan, "Linear systems," Chapt. 7, Lecture notes, University of Auckland (1997).

[79] C. Kittel, "Introduction to solid state physics," Chapter 8, New York, John Wiley & Sons Inc, 6th edition (1986).

[80] G. Leibfried and W. Ludwig, "Theory of anharmonic effects in crystals," Sol. State Phys., 12, 275 (1961).

[81] R. Stolen and K. Dransfeld, "Far-infrared lattice absorption in Alkali Halide crystals," Pyhs. Rev., 139, A1295 (1965).

[82] T. C. McGill, R. W. Hellwarth, M. Mangir and H. V. Winston, "Infrared absorption I ionic insulators due to multiphonon processes," J. Phys. Chem. Solids, 34, 2105 (1973).

[83] B. Szigeti, "Higher-order terms in the dielectric constant of ionic crystals," Proc. Roy. Soc., A252, 217 (1959).

[84] S. Nashima, O. Morikawa, K. Takata and M. Hangyo, "Temperature dependence of optical and electronics properties of moderately doped silicon at terahertz frequencies," J. of Appl. Phys., 90, 837 (2001).

[85] W. L. Wolfe, "Properties of optical materials," Section 7, Handbook of optics, McGraw-Hill Inc., USA (1978).

[86] L. Genzel, H. Happ and R. Weber, "Dispersionsmessungen an NaCl, KCl und KBr zwischen 0,3 und 3 mm Wellenlange," Physik, 154, 13 (1959).

[87] M. E. Thomas, "Temperature dependence of the complex index of refraction," Chapt. 8, Academic Press, Handbook of Optical Constants of Solids II (1991).

[88] A. B. Vasilev and L. D. Kislovskii, "Frequency and temperature dependence of the absorption in the wings of the bands of the characteristic lattice vibrations of dielectrics: 4," Opt. Spectrosc. (USSR) 46, 495 (1979).

[89] H. H. Li, "Refractive index of alkali halides and its wavelength and temperature derivatives," J. Phys. Chem. Ref. Data, 5, 441 (1976).

[90] J. R. Jasperse, A. Kahan and J. N. Plendl, "Temperature dependence of infrared dispersion in ionic crystals LiF and MgO," Phys. Rev., 146, 526 (1966).

[91] J. D. H. Donnay, W. P. Mason and E. A. Wood, "Crystallographic properties," Section 9a, American Institute of Physics Handbook, McGraw-Hill Inc., 3rd edition (1982).

[92] J. D. Edwards, C. S. Taylor, A. S. Russell and L. F. Maranville, "Electrical conductivity of molten Cryolite and Potassium, Sodium, and Lithium Chlorides," J. of Electrochem. Soc., 90, 527 (1952).

[93] J. C. Owens, "Anharmonicity and millimeter-wave absorption in Alkali-Halide crystals," Phys. Rev., 181, 1228 (1969).

[94] J. R. Hardy and A. M. Karo, "Theoretical study of the long-wavelength optical properties of NaCl, KCl, KBr and KI," Phys. Rev. B, 26, 3327 (1982).

[95] M. Schall, "Phononenprozesse und Ladungsträgerdynamik in Halbleitern," Dissertation, Albert-Ludwigs-Universität, Freiburg i. Br., (2001).

[96] Homepage, Center for Ultrafast Optical Science, University of Michigan.

[97] Homepage, Department of Chemistry, Yale University.

Curriculum Vitae

NAME: Noboru HASEGAWA

SEX: Male

DATE OF BIRTH: December 24, 1965

PLACE OF BIRTH: Kobe, Hyogo, Japan

PRESENT ADDRESS: 1-51-14 Oyumino, Midori-ku, Chiba 266-0031, JAPAN

MARITAL STATUS: Married, 3 children

EDUCATION:

  Institute : Osaka University (Osaka, Japan)

      From April 1985 to March 1989, Faculty of Engineering

        Degree : Bachelor of Engineering (March 1989),   Major : Applied Physics

          GPA：   3.84 (by a A=4.00 basis, Special Subject)

               3.16 (by a A=4.00 basis, General Education Subject)

      From April 1989 to March 1991, Division of Engineering, Graduate School

        Degree : Master of Engineering (March 1991),   Major : Applied Physics

          GPA：   3.50 (by a A=4.00 basis)

  Institute : Johann Wolfgang Goethe-Universität, Frankfurt am Main

      From August 2001 to June 2003, Ultrakurzzeitspektroskkopie und Terahertz-Phzsik Lab.   (Prof. H. G. Roskos), Physikalisches Institut

PROFESSIONAL EXPERIENCE:

 (from April 1994 to August 2001, and from July 2003 to date)

   Instrument & Control R&D Div., Environment & Process Technology Center, Nippon Steel Corporation, 20-1 Shintomi, Futtsu, Chiba, 293-8511, JAPAN

SOCIETY MEMBERSHIP: The Applied Physics Society of Japan

                                   The Iron and Steel Institute of Japan

Acknowledgements